SYNTHESIS AND CHARACTERIZATION OF COBALT-SUBSTITUTED FERRITE NANOPARTICLES USING REVERSE MICELLES

By

Victoria L. Calero Díaz del Castillo

A thesis submitted in partial fulfillment of the requirements for the degree of

MASTER OF SCIENCES
In
CHEMICAL ENGINEERING

UNIVERSITY OF PUERTO RICO
MAYAGÜEZ CAMPUS
September, 2005

Approved by:

_____   _____
Carlos Rinaldi, PhD   Date
President, Graduate Committee

_____   _____
Oscar Perales-Perez, PhD   Date
Member, Graduate Committee

_____   _____
Madeline Torres-Lugo, PhD   Date
Member, Graduate Committee

_____   _____
Nelson Cardona-Martínez, PhD   Date
Chair, Chemical Engineering

ABSTRACT

With the objective of developing a magnetic nanoparticle based sensor, we have synthesized cobalt-substituted ferrite particles using reverse micelles. Reverse micelles have been used to control the nanoparticle size. Cobalt ferrite was chosen due to its high anisotropy constant which assures that the relaxation mechanism is Brownina. Fe:Co ratios of 3:1, 4:1, and 5:1 were used in the synthesis, obtaining cobalt-substituted ferrites ($Co_xFe_{3-x}O_4$). Inductively coupled plasma mass spectroscopy (ICP-MS) verified the presence of cobalt in all samples. Fourier transform infrared (FTIR) spectra show bands at ~560 and ~400 cm^{-1}, confirming the metal-oxygen bond characteristic of ferrites. Transmission electron microscopy shows that the average size of the particles was ~3 nm with a geometric deviation of ~0.2. X-ray diffraction (XRD) confirmed the inverse spinel structure typical of ferrites with a lattice parameter of $a = 8.388\,\text{Å}$ for $Co_{0.61}Fe_{0.39}O_4$, which is near that of $CoFe_2O_4$ ($a = 8.39$ Å). Magnetic properties were determined using a Superconducting Quantum Interference Device (SQUID). Coercivities (H_c) higher than 8 kOe were observed at 5 K, whereas at 300K the particles showed superparamagnetic behavior.

The anisotropy constant was determined based on the Debye model for a magnetic dipole in an oscillating field. We obtained an expression relating χ' and the temperature of the in-phase susceptibility peak. Anisotropy constant values in the order of ~10^6 kerg/cm^3 were determined, using the Debye model, whereas anisotropy constants in the order of ~10^7 kerg/cm^3 were calculated assuming $\Omega\tau = 1$ at the temperature peak of the in-phase component of the susceptibility curve.

ACKNOWLEDGEMENTS

I want to thank everyone who shared with me in this period of my life, specially:

Sandra Lima for helping me in taking the first step; Adriana Herrera for her advise, support, and unconditional friendship; Nayla Ayala and her family (Leonor, Hector, Noris y Norbert) for their affection and making me feel as a member of their family; Leonardo Pacheco for his help me with FTIR measurements; Arlex and Carola my labmates; Sandra, Mireily, and Marisol for you friendship.

I specially want to thank my advisor Dr. Carlos Rinaldi for his support, help, and trust. Also because he was and is a friend who trusted in me and gave me the support necessary to finalize my master and to continue my professional development. Thank you.

Gladiz (my mom), Alex (my father), Kelly, Jenny (my sisters and friends), Melba, Victoria (my grandmothers) and Carlos (my uncle) for all their love and support during my life.

CONTENT

LIST OF FIGURES

1. INTRODUCTION

Nanotechnology involves the study, control, and manipulation of materials at the nanoscale, typically having dimensions less than 100 nm. This is a truly multidisciplinary area of research and development, bringing together the disciplines of chemistry, biology, engineering, and medicine. The recent interest in nanostructures results from their numerous potential applications such as in materials development, biomedical sciences, electronics, optics, magnetism, energy storage, and electrochemistry [1].

The emergence of nanotechnology is opening new horizons for the development of nanosensors and nanoprobes with submicron-sized dimensions that are suitable for chemical and biological measurements. To this day, nanosensors have been developed using optical fibers in order to monitor biomolecular processes within a single living cell [2]; based on silver nanoparticles used to identify biotin [3]; composed of a polymer matrix incorporated with fluorescent indicator dyes suitable for the chemical analysis of calcium, potassium, and oxygen [4]; using gold nanoparticles which carry oligonucleotides capable of sensing complementary strands detectable by color changes [5]; and using magnetic nanoparticles to detect molecular interactions (DNA-DNA, protein-protein and enzyme reactions) [5], biotin [6], and glucose [7], among others.

The application of magnetic nanoparticles in sensors [8] has been of great interest as it allows the analysis of turbid samples because the detection method is based on changes in nanoparticle magnetic properties, such as the relaxation time. When the analyte attaches to a functionalized nanoparticle, the particle hydrodynamic size increases causing an increase in the Brownian relaxation time, which can be observed using a magnetometer or AC susceptometer.

Cobalt ferrite has been synthesized using reverse micelles. The interest in this material stems from its high magnetocrystalline anisotropy. The reverse micelle method

1

produces nanoparticles that are spherical with narrow size distribution, important characteristics for application in sensors.

In order to study magnetic nanoparticle based sensors, we have synthesized cobalt-substituted ferrite particles with ~3 nm diameter ($\ln \sigma_g \approx 0.2$) using reverse micelles. Fe:Co ratios of 3:1, 4:1, and 5:1 were used in the synthesis process and techniques such as Transmission Electron Microscopy (TEM), X-Ray Diffraction (XRD), Superconducting Quantum Interference Device (SQUID) magnetometry, and Inductively Coupled Pasma Mass Spectroscopy (ICP-MS) were used to characterize the nanoparticles.

2. OBJETIVES

The objectives of this thesis were to:

1. Synthese cobalt ferrite nanoparticles with controlled size and minimal polydispersity using reverse micelles.

2. Characterize these particles physically, chemically, and magnetically. In particular:

    a. evaluate the degree of incorporation of Co ions into the nanoparticles for various synthesis conditions;
    b. evaluate in the surfactant AOT is easily removed from the particle surface; and
    c. develop a method to determine the value of the magnetic anisotropy of the particles.

3. BACKGROUND

3.1. Theory of Magnetism

Magnetism is a phenomenon through which materials assert an attractive or repulsive force or influence on other materials. One of the fundamental concepts in magnetism is the magnetic field. A field is generated in a volume of space when there is a change in energy of that volume. The force produced by the energy gradient can be detected by the acceleration of an electric charge moving in the field, by the force on a current-carrying conductor, or by the torque on a magnetic dipole [9].

A magnetic field is produced when there is electric charge in motion. Analogous to the electric field, the magnetic effect may be regarded as due to so-called magnetic dipoles in a permanent magnet [9, 10] , or as originating from flowing electrical currents (Oersted, 1819).

3.1.1.   The Bohr theory of magnetism and spin moments

The quantum theory of matter (Niels Bohr, 1913) postulates that the electron orbit around the nucleus of the atom originates the magnetic behavior of matter (Figure 1a). The basic unit of electron magnetism is called the Bohr magneton (μ_B= 9.27x10^{-21} erg/Oe), which is the result of the orbital motion of one electron in the lowest orbit.

However, the Bohr theory did not provide a complete description of the origin of magnetism. In 1925 and 1926, Goudsmit and Uhlenbeck respectively, introduced the concept of electron spin, which better explains the origin of magnetism. Spin corresponds to movement of electric charge in the electron, hence an electric current which produces a magnetic moment in the atom (Figure 1b). The net magnetic moment is the vector sum of the individual spin and orbital moments of the electrons in the outer shells [11].
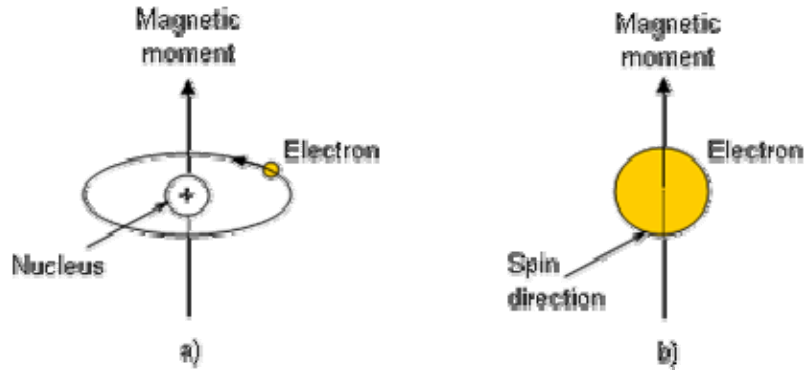
Figure 1: *Classical and quantum origins of magnetism.*

The electron spin may adopt two modes which are commonly represented as arrows pointed up or down. In an atom, mutually opposed paired spins cancel and do not result in magnetic moment, while the unpaired spins will give rise to a net magnetic moment. Each unpaired spin contributes 1 Bohr magneton. Table 1 shows the number of Bohr magnetons for some ions [11].

Table 1: Bohr magneton in ions commonly found in magnetic materials.

Ion	Bohr magneton
	μ_0
Fe^{2+}	5
Fe^{3+}	4
Co^{2+}	3
Ni^{2+}	2
Mn^{2+}	5

3.1.2. Magnetic field and magnetic moment.

A magnetic force is exerted on moving electrically charged particles in a magnetic field [12]. This is called the Lorentz force f and relates a charge q which is moving in the magnetic field B at a velocity v by equation (3.1), as illustrated in Figure 2 [13].

$$f = q \times (v \times B).$$
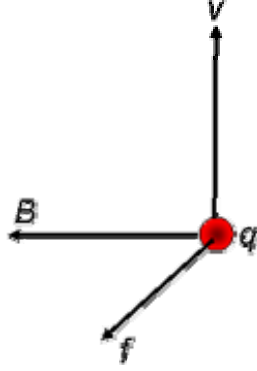
Figure 2: *Lorentz force due to the movement of a charge through a magnetic field.*

Ampère showed that a magnet could be replaced by an equivalent current which exerts forces on other currents. In this manner, the magnetic field can be manipulated easily. The measurements of Ampère were quantified by Biot and Savart by showing that the magnetic field B at a distance r from a charge in movement is

$$B = \frac{\mu_0 qv \times i_r}{4\pi r^2} \ .$$

where μ_0 is the free space permeability ($4\pi \times 10^{-7}$ Henry/m). The SI unit of B is Tesla.

Atomic currents (generated from orbiting electrons and spin contributions) are analogous to the electric dipole and may be considered as resulting from a small circulating current of magnitude I, and loop area dS (Figure 3).
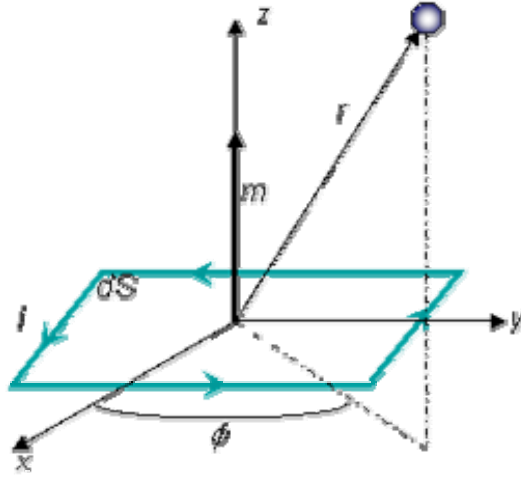
Figure 3: *Schematic of a magnetic dipole whose magnetic moment m is in the direction normal to the loop.*

The magnetic dipole moment *m* is the vector in the direction perpendicular to the loop with magnitude given by

$$m = IdS . \tag{3.1}$$

The resulting magnetic field is

$$B = \frac{\mu_0 m}{4\pi r^3}\left[2\cos\theta \mathbf{i}_r + \sin\theta \mathbf{i}_\theta\right]. \tag{3.2}$$

Equation (3.4) is identical to the field due to an electric dipole when one replaces $\mu_0 m$ by ρ/ε_0.

Ampère postulated that magnetic materials are composed of infinitesimal circulating current loops (Figure 4) with number density *N*. The magnetization vector *M* is defined as the magnetic dipole density:

$$M = Nm = NIdS . \tag{3.3}$$

In SI, M has units of A/m.

As is illustrated in Figure 4, only the dipoles on either side of the edges contribute a net current through the loop.
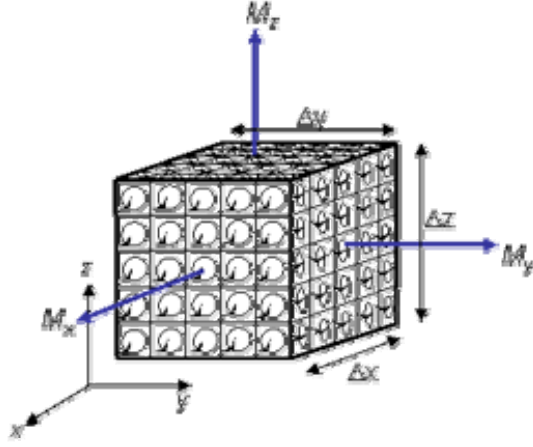
Figure 4: *Model for magnetic materials postulated by Ampère.*

Assuming that the dipoles along the edge do not change magnitude or direction, the total current in the z direction linked by the edges (x and $x + \Delta x$) is given by

$$I_{z\ total} = \Delta x \Delta y \left(\frac{M_y(x+\Delta x) - M_y(x)}{\Delta x} - \frac{M_x(y+\Delta y) - M_x(y)}{\Delta y} \right). \qquad (3.4)$$

If Δx and Δy become small, equation (3.6) can be written as

$$\lim_{\substack{\Delta x \to 0 \\ \Delta y \to 0}} J_z = \frac{I_{z\ Total}}{\Delta x \Delta y} = \left(\frac{\partial M_y}{\partial x} - \frac{\partial M_x}{\partial y} \right) = (\nabla \times \overline{\mathbf{M}})_z, \qquad (3.5)$$

where J_z is the z component of the curl of the magnetization. In general, the current density or Amperian current density (generated by the motion of bound charges in a material) is given by

$$\mathbf{J}_m = \nabla \times \mathbf{M}. \qquad (3.6)$$

8

Considering that magnetic fields can also be generated by these currents, Ampère's law is written as

$$\nabla \times \frac{\mathbf{B}}{\mu_0} = \mathbf{J}_f + \mathbf{J}_m, \tag{3.7}$$

where $\mathbf{J}_f$ is the free current generated by the motion of free charges.

The magnetic field intensity H may be defined with respect to the magnetic flux density B by

$$B = \mu_0(H + M), \tag{3.8}$$

which we may replace in equation (3.9) to obtain

$$\nabla \times \left(\frac{\mathbf{B}}{\mu_0} - \mathbf{M} \right) = \nabla \times \mathbf{H} = \mathbf{J}_f. \tag{3.9}$$

In free space, $\mathbf{M} = \mathbf{0}$ hence $\mathbf{B} = \mu_0 \mathbf{H}$. In SI units of H is A/m.

The free current density $\mathbf{J}_f$ generates the $\mathbf{H}$ field, whereas the magnetization current density $\mathbf{J}_m$ generates the $\mathbf{M}$ field. The total current $(\mathbf{J}_m + \mathbf{J}_f)$ is the source of the B field [13], multiplied by μ_0 to change units.

Another concept commonly encountered is the magnetic flux Φ, which quantifies the magnetic field through a surface

$$\Phi = \int_S B \cdot dS. \tag{3.10}$$

9

3.1.3. Magnetic behavior

Magnetic materials can be classified based on differences between their internal and external flux and the variation of the magnetization M or magnetic induction B when a magnetic field is applied (Figure 5) [12, 14]. There are two quantities that relate M and B to $H:$ the susceptibility χ and the permeability μ :

$$\chi = \frac{M}{H}, \tag{3.11}$$

$$\mu = \frac{B}{H}. \tag{3.12}$$

In SI the permeability μ has units of Henry/m. The susceptibility is a measure of the increase in magnetic moment caused by an applied field, whereas permeability represents the relative increase in flux caused by the presence of the magnetic material [10].

Diamagnetism

Diamagnetism is an inherent result of the orbital motion of the electrons in a magnetic field. It is present when the atom has zero net magnetic moment. In this case the orbital motion generates a field opposite to the applied field (magnetization is directed oppositely to the field, as illustrated in Figure 6), described by a negative susceptibility. These materials tend to move toward regions of weaker field [10, 11].

Paramagnetism

Paramagnetic materials possess a permanent dipole moment due to incomplete cancellation of electron spin and/or orbital magnetic moments. In the absence of an applied magnetic field the dipole moments are randomly oriented, therefore the material has no net macroscopic magnetization. When a field is applied these moments tend to align by rotation towards the direction of the field and the material acquires a net magnetization (Figure 7) [12].
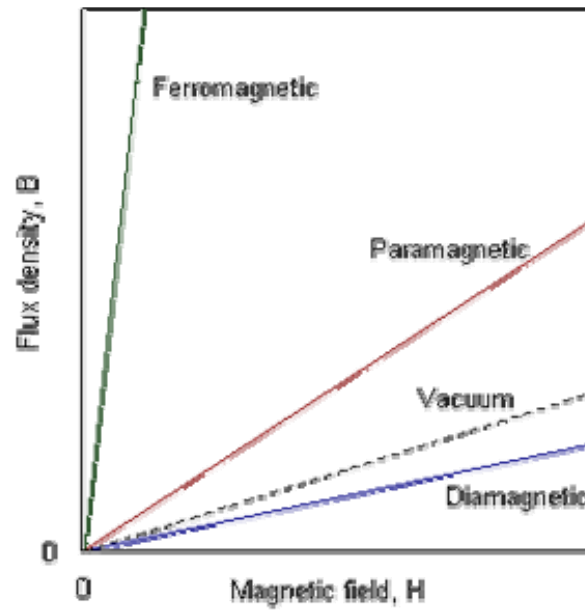
Figure 5: *Representation of the behavior of the flux density with respect to the magnetic field for different classes of magnetic materials.*
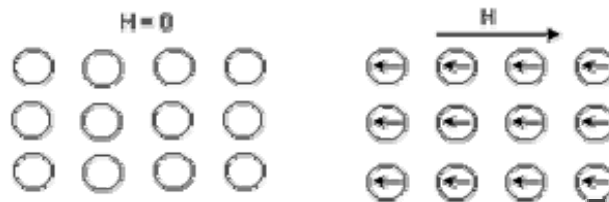
Figure 6: *Atomic dipole configuration for a diamagnetic material.*
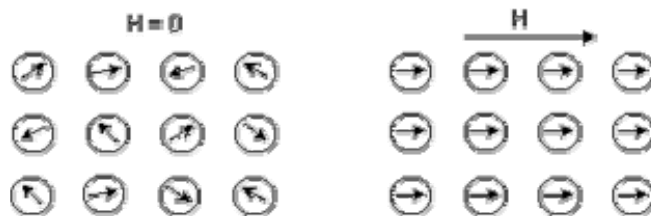
Figure 7: *Schematic of atomic dipoles for a paramagnetic material.*

Ferromagnetism and ferrimagnetism

Ferro and ferri-magnetic materials possess a permanent magnetic moment in the absence of an external field and a very large permanent magnetization [12]. In ferromagnetic materials, this permanent magnetic moment is the result of the cooperative interaction of large numbers of atomic spins in what are called domains, regions where all spins are aligned in the same direction. In ferrimagnetic materials, on the other hand, incomplete cancellation of the magnetic dipoles in a domain results in lower permanent magnetization (Figure 8) [11].
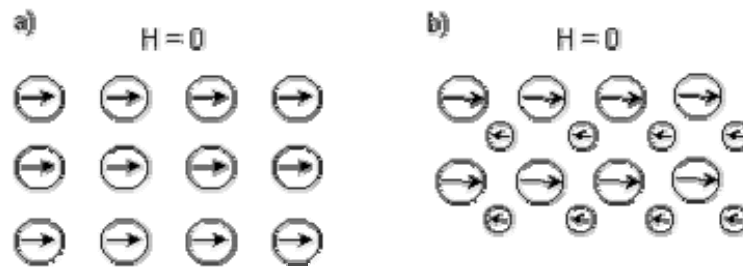
Figure 8: *Ordering of the atomic dipoles in a) ferromagnetic and b) ferrimagnetic material.*

The macroscopic magnetization of ferro- and ferri-materials is the sum of the magnetizations of the domains which make up the sample [12]. Ferrimagnets are ionic solids meaning that they are electrically insulating, whereas most ferromagnets are metals (conductors) [14].

3.1.4. Domains

In 1907 Weiss proposed what is known as the domain theory of magnetism. This theory contends that a ferro- or ferri-magnetic material is composed of domains, each one magnetized to saturation in some direction (the magnetic moments are oriented in a fixed direction) as shown schematically in Figure 9.
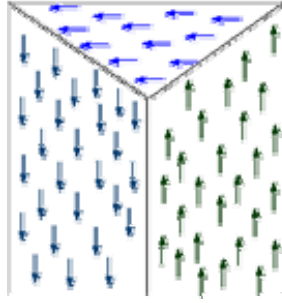
Figure 9: Illustration of domains in ferromagnetic materials.

Domains typically contain from 10^{12} to 10^{15} atoms and are separated by domain boundaries or walls. The formation of domains allows a ferro or ferri-material to minimize its total magnetic energy. The magnetic energy is composed of several types of energy [11, 14]:

a. *Magnetostatic or demagnetization energy*: The magnetized material behaves like a magnet, with a surrounding magnetic field. This field acts to magnetize the material in the direction opposite from its own magnetization, causing a magnetostatic energy which depends on the shape of the material. This magnetostatic energy can be reduced by reducing the net external field through the formation of domains inside the material.

b. *Magnetocrystalline anisotropy energy:* In some materials the domain magnetization tends to align in a particular crystal direction (the so-called easy axis). The material is easiest to magnetize to saturation or demagnetize from saturation if the field is applied along an easy axis. The energy difference between aligning the domain in the easy and another direction (hard direction) is called magnetocrystalline anisotropy energy. Anisotropy energy is the energy needed to rotate the moment from the easy direction to a hard direction. For materials with cubic crystalline structure (such as ferrites), the energy is expressed in terms of anisotropy constants and the direction to which the magnetization rotates.

$$E_k = K_1 \sin^2 \theta + K_2 \sin^4 \theta... \qquad \text{(hexagonal structure)}$$

$$E_k = K_1(\alpha_1^2\alpha_2^2 + \alpha_2^2\alpha_3^2 + \alpha_3^2\alpha_1^2) + K_2(\alpha_1^2\alpha_2^2\alpha_3^2 + ... \quad \text{(cubic structure)}$$

(3.13)

where K is the anisotropy constant, θ is the angle between the easy axis and the direction of magnetization, and α ; are the direction cosines, which are the ratios of the individual components of the magnetization projected on each axis divided by the magnitude of the magnetization. A crystal is higher in anisotropy energy when the magnetization points in the hard direction rather than along the easy direction. The formation of domains permits the magnetization to point along the easy axis, resulting in a decrease in the net anisotropy energy.

c. *Magnetostrictive energy*: In a magnetic field, the material may change its dimensions on the order of several parts per million. This change in dimension results in what is called magnetostrictive energy, which is lowered by a reduction in the size of the domains, requiring the formation of more domains.

d. *Domain wall energy:* This is energy resulting from the increase or decrease in the width of the walls due to the growth/shrinkage of domains.

The magnetization in a domain changes by two mechanisms: rotation of the magnetic dipoles toward the direction of the applied field and change in the domain volume (Figure 9). In the first case, a certain amount of anisotropy energy is needed to rotate the magnetization in a crystal from the easy to another axis. In the second mechanism, the volume of the domain changes, changing its contribution to the bulk magnetization, while the magnetization direction is unchanged. The change in the magnetization intensity of a domain depends on how close its direction is to the direction of the applied field. If the magnetization direction is close, the intensity in the domain increases, whereas if it is far, the intensity decreases.
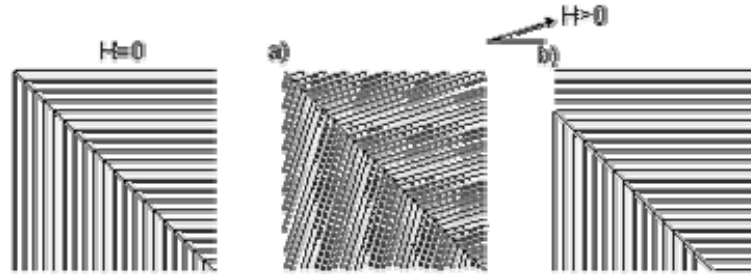
Figure 10: Change of domain magnetization by a) domain rotation and b) domain wall movement.

The domain volume changes due to motion of the domain wall. This movement is originated by a torque that rotates the moments of the domain in line with the field, moving the center of the wall toward the domain opposed to the field. Consequently, the volume of the domains whose direction is favorable is increased whereas the domains with unfavorable direction decrease in volume [11].

3.1.5. Magnetization curve and hysteresis loops

The magnetization curve describes the change in magnetization or magnetic flux of the material with the applied field. When a field is applied to a material with randomly oriented magnetic moments, it will be progressively magnetized due to movement of domain boundaries. Initially, when no field is applied, the magnetic dipoles are randomly oriented in domains, thus the net magnetization is zero. When a field is applied, the domains begin to rotate, increasing their size in the case of the domains with direction favorable with respect to the field, and decreasing for the domains with unfavorable direction. As the field increases, the domains continue to grow until the material becomes a single domain, which is oriented in the field direction. At this point, the material has reached saturation (Figure 11) [12].

As the magnetic field is increased or decreased continuously, the magnetization of the material increases or decreases but in a discontinuous fashion. This phenomenon is

15

called the Barkhausen effect and is attributed to discontinuous domain boundary motion and the discontinuous rotation of the magnetization direction within a domain [9].

The typical magnetization curve can be divided into three regions:

a. Reversible region: The material can be reversibly magnetized or demagnetized. Charges in magnetization occur due to rotation of the domains with the field.

b. Irreversible region: Domain wall motion is irreversible and the slope increases greatly.

c. Saturation region: Irreversible domain rotation. It is characterized by a required large amount of energy to rotate the domains in the direction of the field [11].
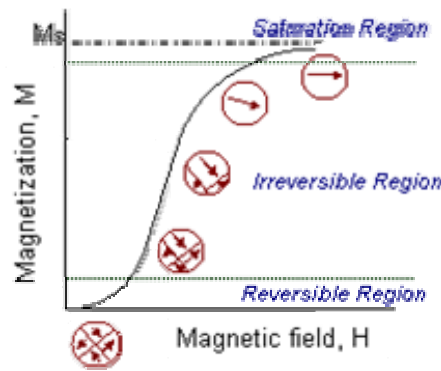
Figure 11: Magnetization curve with domain configurations at different stages of magnetization.

If the field is reduced from saturation, with eventual reversal of field direction, the magnetization curve does not retrace its original path, resulting in what is called a hysteresis loop. This effect is due to a decrease of the magnetization at a lower rate. The area inside the hysteresis loop is indicative of the magnetic energy losses during the magnetization process. When the field reaches zero, the material may remain magnetized (i.e., some domains are oriented in the former direction). This residual magnetization is commonly called remanence M_r. To reduce this remanent magnetization to zero, a field with opposite direction must be applied. The magnitute of field required to lower the sample magnetization to zero is called the coercivity H_c (Figure 12).

A material can present different hysteresis loops depending on the degree of magnetization. If the maximum magnetization is less than the saturation magnetization, the loop is called a minor loop [12, 14].

3.2. Ferrites

The most important ferrimagnets are the materials known as ferrites. Ferrites are ferrimagnetic oxides and therefore are electrically insulating. Ferrites are widely used in high-frequency applications, because an AC field does not induce undesirable eddy currents in an insulating material [12, 14].
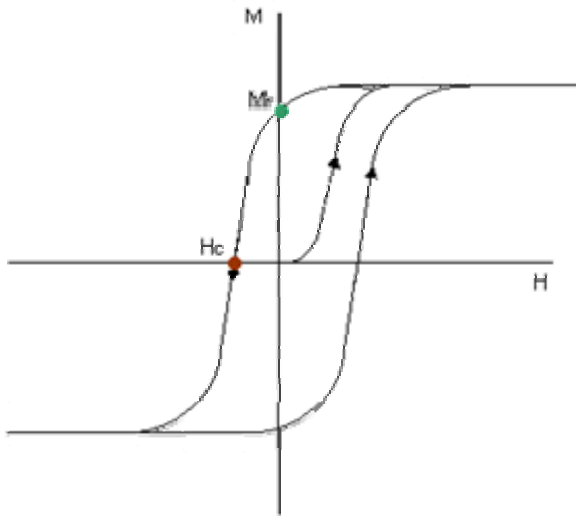
Figure 12: Schematic of a hysteresis loop.

Ferrites have two different structural symmetries which are determined by the size and charge of the metal ions that balance the charge of the oxygen ions, and their relative amounts [11].

3.2.1. Cubic ferrites

The cubic ferrite has the general formula $MO \cdot Fe_2O_3$ where M is a divalent ion. These ferrites crystallize in the spinel structure. The spinel lattice is composed of a close-packed oxygen arrangement in which 32 oxygen ions form the unit cell (the smallest repeating unit in the crystal network). These anions are packed in a face centered cubic (FCC) arrangement leaving two kinds of spaces between anions: tetrahedrally coordinated sites (A), surrounded by four nearest oxygen atoms, and octahedrally coordinated sites (B), surrounded by six nearest neighbor oxygen atoms. These are illustrated in Figure 13. In total, there are 64 tetrahedral sites and 32 octahedral sites in the unit cell, of which only 8 tetrahedral sites and 16 octahedral sites are occupied, resulting in a structure that is electrically neutral [11, 14].
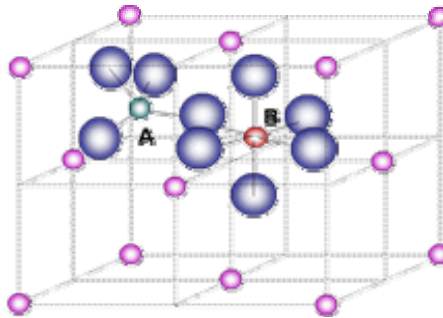
Figure 13: Schematic of two subcells of a unit cell of the spinel structure, showing octahedral and tetrahedral sites.

The localization of ions either in the A or B sites depends fundamentally on the ion and lattice sizes. Also it has been observed to depend on the temperature and the orbital preference for specific coordination.

In general, divalent ions are larger than trivalent ions (Table 2). This is because trivalent ion nuclei produce greater electrostatic attraction, hence their electron orbits contract. The octahedral sites are larger that the tetrahedral sites, thus, the divalent ions are localized in the octahedral sites whereas trivalent ions are in the tetrahedral sites [11].

The distance and angle between the metals and oxygen atoms in the spinel structure are given in Figure 14 [11].

There are two spinel structures: normal and inverse. In the case of the normal spinel, the divalent ions are all on A sites and trivalent ions occupy B sites. A majority of these ferrites present paramagnetic behavior. In the inverse spinel, the divalent ions occupy only B sites while trivalent ions are located on both A and B sites in equal proportion. The spin moments of the trivalent ions in an inverse spinel are canceled (direction of moment on A sites is opposed to B sites) whereas the spin moments of the divalent ions are aligned, resulting in a net magnetic moment [14].

The cubic ferrite is easily magnetized and demagnetized; it has high permeability and saturation magnetization, low electrical conductivity, and the anisotropy energy is dominated by K_1. If K_1 is greater than zero, the easy direction is the cube edge direction (100) whereas if K_1 is less than zero, the body direction is preferred (111). For most ferrites the value of K_1 is negative, with the exception of cobalt ferrite [11].

Table 2: Radii of metal ions commonly involved in spinel ferrites.

Ion	Ionic radius Å
Fe^{2+}	0.83
Fe^{3+}	0.67
Co^{2+}	0.82
Zn^{2+}	0.74
Ni^{2+}	0.78
Mn^{3+}	0.70

Ferrites are characterized by square-shaped hysteresis loops, which originate from their large magnetocrystalline anisotropy. Additionally, they have short relaxation times, minimal mechanical strength, and low magnetostriction [14].

19
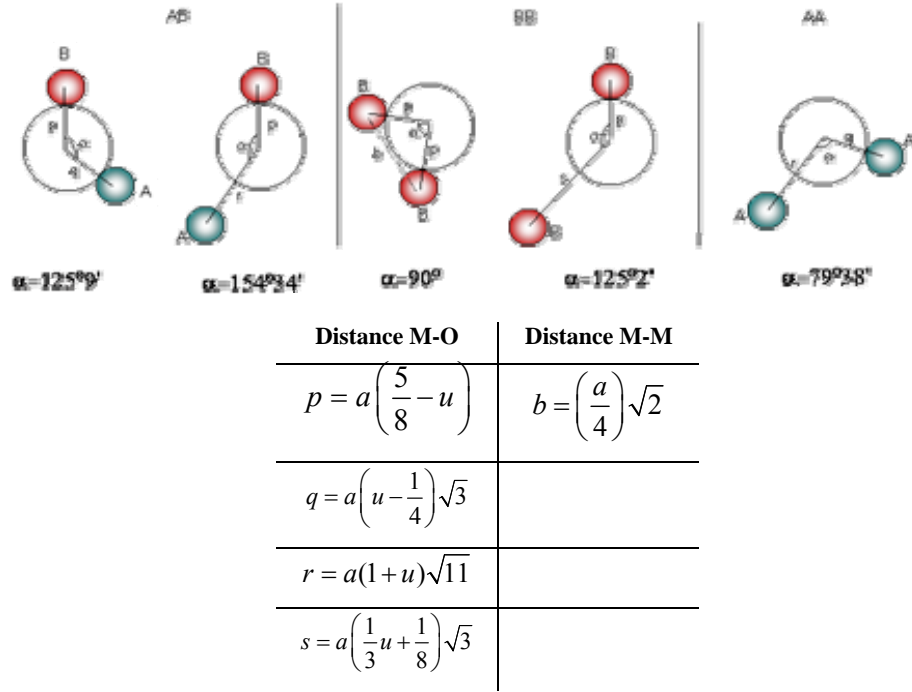
Figure 14: *Interionic distances and angles in the spinel structure for the different types of lattice site interactions*

.

3.2.2. Hexagonal ferrites

Hexagonal ferrites are widely used as permanent magnets and are characterized by possesing a high coercivity [14]. Their general formula is $MO \cdot 6Fe_2O_3$ where M can be Ba, Sr, or Pb. The hexagonal ferrite lattice is similar to the spinel structure, with the oxygen ions closely packed, but some layers include metal ions, which have practically the same ionic radii as the oxygen ions. This lattice has three different sites occupied by metals: tetrahedral, octahedral, and trigonal bi pyramid (surrounded by five oxygen ions).

3.2.3. Cobalt ferrite

Some properties of the ferrites can be enhanced by incorporation of divalent metallic ions inside their structure. In the case of cobalt ferrite, the incorporation of cobalt

ions results in an increase in coercivity due to an increased magnetocrystalline anistotropy resulting from the coupling of the spins of the cobalt and iron ions [11, 15].

Cobalt ferrite ($CoFe_2O_4$) is a cubic ferrite with inverse spinel structure where Co^{+2} ions are located in B sites and Fe^{+3} in the A and B sites. The unit cell is characterized by a length of 8.38 Å and the interaction distances from Figure 14 are b= 2.963 Å, u= 0.2714 Å, p=2.963 Å, q= 0.3106 Å, r=38.336 Å and s=3.127 Å [11]. This ferrite is characterized by having an anisotropy constant higher than the common ferrites (Table 1.3) such as magnetite and maghemite. The anisotropy constant of bulk cobalt ferrite is in the range of 1.8 to 3.0 x 10^6 erg/cm^3 and the saturation magnetization is 80.8 emu/g at room temperature and 93.9 emu/g at 5 K [16].

Table -3: Anisotropy constants of some ferrites [11].

Ferrite	Anisotropy constant K_1 (erg/cm^3)
$FeFe_2O_4$	-1.1×10^3
$Co_{0.8}Fe_{2.2}O_4$	3.9×10^6
$MnFe_2O_4$	-28×10^3
$Co_{0.3}Mn_{0.4}Fe_2O_4$	1.1×10^6

It has been observed that the magnitude of magnetic properties depends on the particle size. A decrease in particle size results in a decrease in coercivity and saturation magnetization whereas the susceptibility and anisotropy constant have been reported to increase. For particles with diameter of 2 nm (determined by TEM) $M_s = 14$ emu/g, $H_c = 5$ kOe, $\chi = 2 \times 10^{-4}$ Oe and $K_a = 7 \times 10^7$ erg/cm^3 while for particles with 5 nm diameter $M_s = 35$ emu/g, $H_c = 9$ kOe, $\chi = 4 \times 10^{-4}$ Oe and $K_a = 1 \times 10^7$ erg/cm^3 [17].

3.3. Ferrofluids

The planned magnetic nanoparticles based sensor consist of utilizing the particles in a stable colloidal dispersion which is commonly called ferrofluid. The particles are coated by surfactant/polymer dispersant layers of approximately 2 nm thickness which prevent agglomeration of the particles. The coated particles are suspended in the fluid and undergo rotational and translational Brownian motion (illustrated in Figure 15) [18].

Ferrofluids retain the properties of a fluid even in the presence of high magnetic fields, in which particles do not separate from the carrier liquid [19]. These fluids can be used in a great variety of applications such as (i) magneto-responsive colloidal extractants [20], (ii) targeted drug delivery vectors [21, 22], (iii) magnetocytolysis agents for treatment of localized cancerous tumors [1, 23], and (iv) in magnetic cell sorting schemes [24]. Aditionally, ferrofluids have the capability to funtionalize their surfaces for specific applications, such as in nanosensors [8]. Various researchers have focused on developing sensors for biological targets, where the nanoparticles are coated with a dispersant bound to an analyte-specific ligand [8, 25].
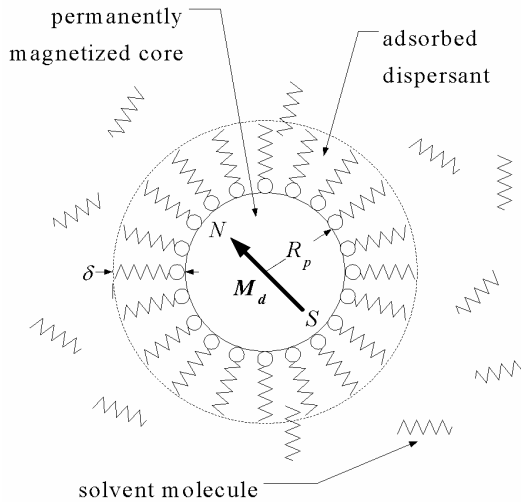
Figure 15:   Ferrofluid as a colloidal dispersion of permanently magnetized nanoparticles of radius R_p possessing a permanent dipole moment with domain magnetization M_d. A stabilizing dispersant layer of thickness δ is adsorbed on the magnetic particle's surface [26].

3.3.1. Stability

An important factor in the application of ferrofluids is their colloidal stability. Stability is determined by the balance between various forms of energy, such as thermal energy $k_B T$, where $k_B = 1.38 \times 10^{-23} \mathrm{\,N\,m\,K^{-1}}$ is Boltzmann's constant and T is the absolute temperature; magnetic energy $\mu_0 MHV$, where V is the volume of the spherical particle, H is the magnetic field, and M is the intensity of magnetization; and gravitational energy $\Delta\rho VgL$, where L is the characteristic height of the container, g is the gravitational force and $\Delta\rho$ is density [18].

Stability of a ferrofluid in a magnetic-field gradient

When a magnetic field is applied to a ferrofluid, the nanoparticles are attracted to the higher-intensity regions of the magnetic field, while thermal energy counteracts the field force and provides statistical motions that allow the particle to remain dispersed throughout the fluid volume. In order for the ferrofluid to remain stable and avoid segregation of the particles in a magnetic field gradient, the ratio of the thermal energy to the magnetic energy must be high

$$\frac{kT}{\mu_0 MHV} \geq 1 , \tag{3.14}$$

thus the maximum particle size must obey

$$d \leq \left(\frac{6kT}{\pi\mu_0 MH} \right)^{1/3} , \tag{3.15}$$

where d is the particle diameter. Experimentally, one can tell a ferrofluid is stable when the nanoparticles spontaneously redistribute throughout the fluid volume over a period of time after the field is removed [18].

Stability against settling in a gravitational field.

The particles in a ferrofluid are constantly pulled downward by gravity but remain dispersed in the fluid by thermal agitation. The ratio between gravitational energy and magnetic energy indicates which mechanism would favor the segregation of the particles. If

$$\frac{\Delta\rho gL}{\mu_0 MH} << 1,$$ (3.16)

the segregation of the particles is mainly due to the magnetic field [18]. This relation is usually satisfied.

Stability of a ferrofluid against magnetic agglomeration

A typical colloidal magnetic fluid contains on the order of 10^{23} particles per cubic meter, hence interparticle collisions are frequent. If the particles were to adhere after collision one would have rapid agglomeration, resulting in cluster growth and eventual instability with respect to segregation in a magnetic field gradient. However, particle-particle adhesion is prevented by various phenomena, depending on the type of dispersant used. When two particles are in contact, these can be separated by applying an energy called the dipole-dipole contact energy, given by

$$E_{dd} = \frac{1}{12}\mu_0 M^2 V .$$ (3.17)

These agglomerates can be broken by thermal agitation; stability against agglomeration is therefore given by the ratio between thermal energy and dipole-dipole contact energy

$$\frac{12kT}{\mu_0 M^2 V} \geq 1,$$ (3.18)

thus the particle size to avoid agglomeration must obey

$$d \leq \left(\frac{72kT}{\pi\mu_0 M^2} \right)^{1/3}.$$

(3.19)

When surfactants are used to stabilize the ferrofluid, adhesion due to van der Waals forces typically is prevented. The van der Waals forces spontaneously arise between neutral particles due to fluctuations in electric dipole-dipole interactions (see Figure 16). This force represents the quantum-mechanical interaction arising from fluctuating orbital electrons in one particle inducing oscillating dipoles in the other. The van der Waals force depends on the interparticle distance, being repulsive at close range and attractive at intermediate to long range (Figure 17).
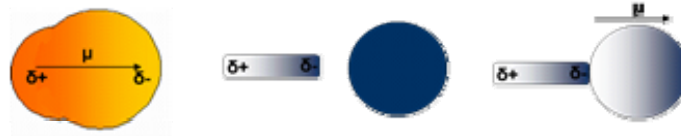
Figure 16:   a) van der Waals forces are generated by attraction between induced dipoles. Dipoles are generated by charge separation: asymmetric distribution of the electric density in the molecule creating δ^- and δ^+ poles. b) The charges on the dipole result in an electrostatic attractive force between molecules.

Steric repulsion is used to prevent particles from approaching so close to one another that van der Waals attraction prevails. This is achieved by the presence of long chain molecules adsorbed onto the particle surface which act as elastic bumpers (Figure 15). The polar groups of the adsorbed species associate with the particle surface either physically or chemically and disguise the surface to look like part of the fluid. Thus, the tails are chosen with properties similar to the surrounding fluid matrix and must be 1-2 nm in length.
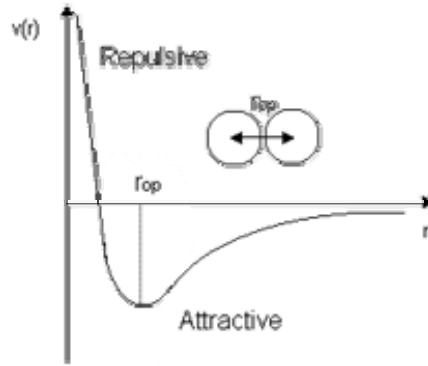
Figure 17: van deer Waals potential energy. When two uncharged molecules or atoms approach one another from a distance there exists a mildly attractive force, but a strongly repulsive force results when they approach too close.

Dispersion of the ferrofluid is determined by the sum of interactions due to van der Waals attractive energy, magnetic attractive energy, and steric repulsion energy. When the net potential energy curve (Figure 18) presents an energy barrier which exceeds the average thermal energy, few particles will cross the barrier resulting in negligible agglomeration [18].
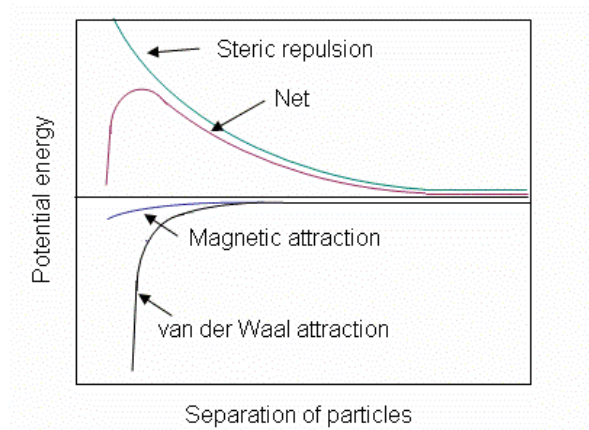
Figure 18: Potential energy vs. separation distance of sterically protected colloidal particles.

3.3.2. Equilibrium magnetization of monodisperse ferrofluids

In the absence of a magnetic field, the particles in a ferrofluid are randomly oriented. When a field is applied, the particles tend to align with the field direction until they achieve their saturation magnetization at high field. Langevin's theory provides a

relation between the net magnetization and the magnetic moments of the suspended particles, assuming that magnetic interaction between the particles is negligible. The energy spent in rotating the particle to align with the field direction is given by

$$W = -m \cdot H = -mH \cos\theta. \tag{3.20}$$

where θ is the angle between the magnetization vector M and applied field H, and m is the particle magnetic moment (Figure 19). The total magnetization for a monodisperse ferrofluid containing n particles per unit volume is

$$M = \frac{n\overline{m}}{\mu_0}, \tag{3.21}$$

where $\overline{m}$ is the component in the field direction of the effective dipole moment of a particle.
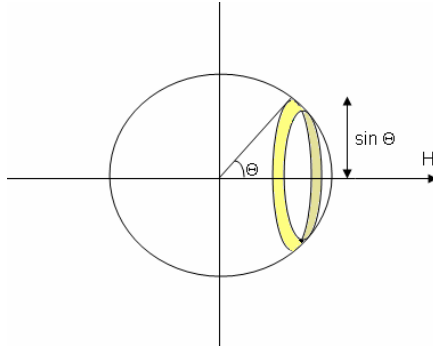
Figure 19: Orientational configuration space for N independent particles.

In the absence of a magnetic field, the number of moments oriented between θ and $\theta + d\theta$ is given by

$$n(\theta)d\theta = N\frac{(2\pi\sin\theta d\theta)}{4\pi(1)^2} = \frac{N}{2}\sin\theta d\theta, \tag{3.22}$$

where N is the total number of moments and $n(\theta)$ is the angular distribution function. When a magnetic field is applied, the probability of finding a particle in a given

27

orientation is proportional to the Boltzmann factor $e^{-W/k_B T}$. Then, the number of moments between angles θ and $\theta + d\theta$ is

$$n(\theta)d\theta \;\propto\; \frac{N}{2}e^{-W/kT}\sin\theta d\theta . \tag{3.23}$$

The effective dipole moment of a collection of particles is given by

$$\overline{m} = \frac{\int_0^\pi m\cos\theta\, n(\theta)d\theta}{\int_0^\pi n(\theta)d\theta} . \tag{3.24}$$

Substituting equations (3.25) and (3.22) in (3.26) we obtain

$$\overline{m} = \frac{\int_0^\pi m\cos\theta\sin\theta \exp\left(\dfrac{mH\cos\theta}{kT}\right)d\theta}{\int_0^\pi \sin\theta \exp\left(\dfrac{mH\cos\theta}{kT}\right)d\theta} . \tag{3.25}$$

Introducing the energy ratio $\alpha = \dfrac{mH}{kT}$ in (3.27) results in

$$\overline{m} = \frac{\int_0^\pi m\cos\theta \exp\left(\alpha\cos\theta\right)d\cos\theta}{\int_0^\pi \exp\left(\alpha\cos\theta\right)d\cos\theta} , \tag{3.26}$$

which upon integration gives

$$\overline{m} = m\left(\coth\alpha - \frac{1}{\alpha}\right) \equiv mL(\alpha) , \tag{3.27}$$

where $L(\alpha)$ is the Langevin function.

The total magnetization for a ferrofluid can be expressed in terms of the domain magnetization using $\mu_0 M_s = nm$ and $M_s = \phi M_d$. Equation (3.23) can be written as

$$\frac{M}{\phi Md} = \frac{\overline{m}}{m} = \coth \alpha - \frac{1}{\alpha} \qquad (3.28)$$

The particle size of ferrofluids can be determined through analysis of the asymptotic values of the Langevin function. At low field, the magnetization curve will display linear behavior, described by (3.31)

$$M = \chi_i H; \quad \chi_i = \frac{\pi \phi \mu_0 M_d^2 d^3}{18kT}, \qquad (3.29)$$

where χ_i is the initial susceptibility. If χ_i is appreciable, the interaction between particles is significant, thus a correction to equation (3.30) must be included. Shliomis (1974) proposed such a correction, assuming monodisperse particles

$$\frac{\chi_i(2\chi_i + 3)}{\chi_i + 1} = \frac{\pi \phi \mu_0 M_d^2 d^3}{6kT}. \qquad (3.30)$$

Approaching saturation (high field), a graph of M vs $1/H$ will be governed by equation (3.33)

$$M = \phi M_d \left(1 - \frac{6kT}{\pi \mu_0 M_d d^3} \frac{1}{H} \right). \qquad (3.31)$$

Upon comparison with experiments, the diameter determined by equation (3.33) is smaller than that determined by equation (3.31). This is because at low field the contribution to the magnetization is made predominantly by larger particles while at high field, the contribution is due to the small particles.

3.3.3. Effect of polydispersity on magnetic equilibrium

The magnetic properties of a ferrofluid are influenced by the particle size and size distribution. Chantrell *et al.* (1978) [27] studied the effect of polydispersity on magnetic properties and presented a method by means of which the median particle diameter and geometric deviation could be determined using a lognormal distribution for the particle size.

Assuming the equilibrium orientation of a single dipole (equation 3.23) still applies for each dipole and using the volume distribution of the particle size $n_V(D_p)$, the magnetization is given by

$$M = M_d \int_0^\infty L(\alpha) n_V(D_p) dD_p \,,$$

(3.32)

where $n_V(D_p) dD_p$ is the volume fraction of particles having diameter D_p to $D_p + dD_p$ and the total volume fraction of particles ϕ is given by

$$\int_0^\infty n_V(D_p) dD_p = \phi \,.$$

(3.33)

Introducing ϕ in equation (3.34) we obtain

$$\frac{M}{M_s} = \frac{\int_0^\infty L(\alpha) n_V(D_p) dD_p}{\int_0^\infty n_V(D_p) dD_p} \,.$$

(3.34)

Chantrell *et al* (1978) [27] and Popplewel *et al* (1995) [28] showed that the particle size distribution of a ferrofluid may be described using a lognormal distribution.

In this case, it is assumed that $\ln D_p$ is normally distributed with mean $\ln \overline{D}_{pg}$ and standard deviation $\ln \sigma_g$

$$n_V(D_p) = \frac{N\sqrt{\pi}}{6\sqrt{2}D_p \ln \sigma_g} \exp\left(-\frac{\ln^2(D_p / \overline{D}_{pgv})}{2\ln^2 \sigma_g} + 3\ln \overline{D}_{pg} + \frac{9}{2}\ln^2 \sigma_g\right), \qquad (3.35)$$

where N is the particle number per volume, $\overline{D}_{pg}$ is the "number" median diameter (half of the particles have a diameter less than $\overline{D}_{pg}$), $\overline{D}_{pgv}$ is the "volume" median diameter (half of the particles have a volume less than that of a particle of diameter $\overline{D}_{pgv}$) and σ_g is the shape parameter or geometric deviation (95% of the particle diameters lie between $\overline{D}_{pg} \Big/ 2\sigma_g$ and $2\overline{D}_{pg}\sigma_g$). $\overline{D}_{pg}$ is related to $\overline{D}_{pgv}$ through equation (3.38)

$$\ln \overline{D}_{pgv} = \ln \overline{D}_{pg} + 3\ln^2 \sigma_g . \qquad (3.36)$$

For the lognormal distribution, one obtains

$$\int_0^\infty n_V(D_p)dD_p = \frac{\pi}{6}\exp(3\ln \overline{D}_{pg} + 9/2\ln^2 \sigma_g)N . \qquad (3.37)$$

Rearranging equation (3.36) [27] results in

$$\frac{M}{M_s} = \int_{^\wedge 0}^\infty \frac{L(\alpha)}{\sqrt{2\pi}D_p \ln \sigma_g} \exp\left(-\frac{\ln^2(D_p/\overline{D}_{pgv})}{2\ln^2 \sigma g}\right)dD_p . \qquad (3.38)$$

At low field, the equilibrium magnetization is given by

$$\lim_{H\to 0}\frac{M}{H} = \frac{\pi\phi\mu_0 M_d^2}{18kT}\int_0^\infty \frac{D_p^3}{\sqrt{2\pi}D_p \ln \sigma_g} \exp\left(-\frac{\ln^2(D_p/\overline{D}_{pgv})}{2\ln^2 \sigma_g}\right)dD_p , \qquad (3.39)$$

31

whereas for high fields it is

$$\lim_{H \to \infty} M = \phi M_d \left[\int \left(1 - \frac{6kT}{\pi \mu_0 M_d H D_p^3} \right) \frac{1}{\sqrt{2\pi} D_p \ln \sigma_g} \exp\left(-\frac{\ln^2 (D_p / \overline{D}_{pgv})}{2 \ln^2 \sigma_g} \right) dD_p \right]. \quad (3.40)$$

Taking $y = D_p / \overline{D}_{pgv}$, equations (3.41) and (3.42) reduce to

$$\lim_{H \to 0} \frac{M}{H} = \chi_0 = \frac{\pi \phi \mu_0 M_d^2 \overline{D}_{pgv}^3}{18kT} \int_0^\infty \frac{y^3}{\sqrt{2\pi} y \ln \sigma_g} \exp\left(-\frac{\ln^2 y}{2 \ln^2 \sigma_g} \right) dy, \quad (3.41)$$

$$\lim_{H \to \infty} M = \phi M_d \left[1 - \frac{6kT}{\pi \mu_0 M_d H \overline{D}_{pgv}^3} \int_0^\infty \frac{y^{-3}}{\sqrt{2\pi} y \ln \sigma_g} \exp\left(-\frac{\ln^2 y}{2 \ln^2 \sigma_g} \right) dy \right]. \quad (3.42)$$

Evaluating the integral

$$\int_0^\infty \frac{y^{\pm 3}}{\sqrt{2\pi} y \ln \sigma_g} \exp\left(-\frac{\ln^2 y}{2 \ln^2 \sigma_g} \right) dy = \exp\left(\frac{9}{2} \ln^2 \sigma_g \right), \quad (3.43)$$

and replacing it in equations (3.43) and (3.44) gives

$$\chi_0 = \frac{\pi \phi \mu_0 M_d^2}{18kT} \overline{D}_{pgv}^3 \exp\left(\frac{9}{2} \ln^2 \sigma_g \right), \quad (3.44)$$

$$\lim_{H \to \infty} M = \phi M_d \left[1 - \frac{6kT}{\pi \mu_0 M_d H \overline{D}_{pgv}^3} \exp\left(\frac{9}{2} \ln^2 \sigma_g \right) \right]. \quad (3.45)$$

Solving for the median diameter and standard deviation finally yields

$$\overline{D}_{pgv} = \left[\frac{18kT}{\pi \mu_0 M_d} \sqrt{\frac{\chi_0}{3\phi M_d H_0}} \right]^{1/3}, \quad (3.46)$$

32

$$\ln \sigma_g = \frac{1}{3} \left[\ln \left(\frac{3\chi_0 H_0}{\phi M_d} \right) \right]^{1/2} , \tag{3.47}$$

where H_0 is the value of H when $M = 0$ at high field, and ϕM_d is the intercept of the curve M vs $1/H$ at $H \to \infty$.

3.3.4. Effect of inter-particle interactions

The expressions for magnetic properties and particle size described above were determined considering negligible particle-particle interaction. Bradbury *et al* (1984) [29] studied the effect of interactions on the magnetic response of a ferrofluid and demonstrated that particle-particle interaction can introduce errors in the parameters determined through magnetic analysis. Using Monte Carlo simulations, Bradbury *et al* [29] found that at low fields, the variation of the initial susceptibility (χ_0) with temperature follows a Curie-Weiss like behavior

$$\chi_i = \frac{\pi \phi \mu_0 M_d^2 d^3}{18 k(T - T_0)} , \tag{3.48}$$

where T_0 is the ordering temperature, a measure of the interparticle interaction strength. At high fields, Monte Carlo simulations showed that magnetization is independent of the particle-particle interaction. From equation (3.50) and using a lognormal distribution as before, the median diameter and standard deviation are now given by

$$\overline{D}_{pgv} = \left[\frac{18k}{\pi \mu_0 M_d} \sqrt{\frac{\chi_0 T(T - T_0)}{3\phi M_d H_0}} \right]^{1/3} , \tag{3.49}$$

$$\ln \sigma_g = \frac{1}{3} \left[\ln \left(\frac{3\chi_0 (T - T_0) H_0}{\phi M_d T} \right) \right]^{1/2} . \tag{3.50}$$

33

3.3.5. Magnetic relaxation

There are two commonly accepted mechanisms by which the magnetization of a colloidal ferrofluid relaxes after the applied magnetic field has changed. In the first mechanism relaxation occurs by particle rotation in the liquid, i.e., the magnetic dipole is locked as the particle undergoes rigid body rotation. In the second mechanism relaxation is due to rearrangement of the magnetic dipole vector within the particle, i.e., the dipole jumps from one easy axis to another.

In the first mechanism, particle rotation occurs due to rotational Brownian motion and is characterized by a Brownian rotational diffusion time τ_B of hydrodynamic origin given by

$$\tau_B = \frac{3V_h \eta_0}{kT},$$
(3.51)

where V_h is the particle hydrodynamic volume and η_o the viscosity of the carrier liquid.

In the absence of a field the magnetization of a single-domain uniaxial ferromagnetic particle can have two possible orientations: the opposing directions along the easy axis of magnetization. In order to move from one to the other, an energy barrier must be overcome. The height of this energy barrier is given by KV, where K is the anisotropy constant of the material and V is the magnetic core volume. When the thermal energy is large enough ($KV \ll kT$), magnetization fluctuations inside the particle are induced with a characteristic time τ_N. This relaxation mechanism was first conceived by Néel and its characteristic time is given as

$$\tau_N = \tau_0 \exp\left(\frac{KV}{kT}\right),$$
(3.52)

where τ_0 is a characteristic time, typically having the approximate value 10^{-9} s.

Depending on the relaxation mechanism of the ferrofluid, it can be said to possess intrinsic or extrinsic superparamagnetism. A suspension possesses intrinsic superparamagnetism when relaxation occurs by the Néel mechanism ($\tau_N \ll \tau_B$). If the relaxation is dominated by the Brownian mechanism ($\tau_B \ll \tau_N$), the suspension is said to exhibit extrinsic superparamagnetism. A material with relaxation time is much greater than the time of the experiment, is called ferromagnetic [18]. Because τ_N has an exponential dependence on V, it is sharply dependent on particle size [30], therefore for the same magnetic material and carrier fluid, the dominant mechanism will depend on the particle size.

3.4. Reverse micelles

Among the various methods for synthesizing magnetic nanoparticles are wet-grinding, co-precipitation, and reverse micelle techniques. The last method has gained recent interest. Reverse micelles consist of aqueous nanometer-sized droplets that are separated form the bulk organic phase by a surfactant layer (Figure 20) [19]. This is an isotropic and thermodynamically stable macroscopically single-phase system that consists of three components: water, oil, and an amphiphillic molecule, the surfactant [31]. In this approach, the micelles play the role of nanoreactors which provide control over particle growth, shape, inter-particle spacing, and produce highly uniform morphologies. Depending on the size of the micelle, particles typically range from 2-10 nm in diameter and their magnetic behavior can range from superparamagnetic to ferromagnetic at larger size [32].

3.4.1. Surfactants

Surfactants are molecules that possess a hydrophilic head group and a hydrophobic tail group. They can be anionic, cationic, or nonionic in nature. All of these factors contribute to the behavior of surfactants in solution. Surfactants have a tendency

to self-assemble into structures that are dependent upon their character and environment. These structures can be spheres, cylinders, ellipsoids, bilayers, vesicles, hexagonal liquid crystals, lamellar sheets, wormlike entanglements, or intercontigous networks, depending on the hydrophobic and hydrophilic interactions at the hydrophilic-water interface [33]. A surfactant molecule lowers the interfacial tension between water and oil resulting in the formation of a transparent or translucent solution [34].
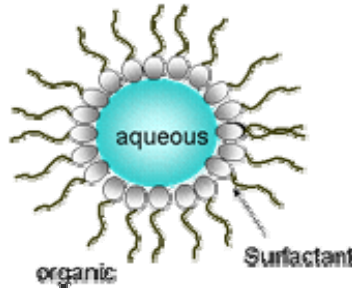
Figure 20: Schematic of reverse micelle.

The surfactant can, spontaneously, form aggregates whose geometry is determined by the packing parameter $v/a_o l_c$, where a_o is the optimal surface area, v the volume, and l_c the effective length of the hydrocarbon chains (Figure 2) [35].

The optimal surface area is the area per headgroup for which the hydrophobic and hydrophilic interactions are balanced, thus the total interface free energy is a minimum. The interfacial free energy μ (equation 3.55) is the sum of the contributions due to positive interfacial free energy per unit area $(\gamma = 50 \text{ mJ/m}^2)$ for the hydrocarbon-water interface, of the hydrophobic interaction (hydrocarbon chain), steric, hydration force and electrostatic contribution of the hydrophilic interaction (headgroup) [36]

$$\mu = \gamma a + \frac{e^2 D}{2\varepsilon a}, \tag{3.53}$$

36

where e is the charge per surfactant molecule, D the thickness of the double layer, and ε the local dielectric constant. Minimizing μ with respect to a gives

$$a_0 = \sqrt{\frac{e^2 D}{2\varepsilon\gamma}} \, . \tag{3.54}$$
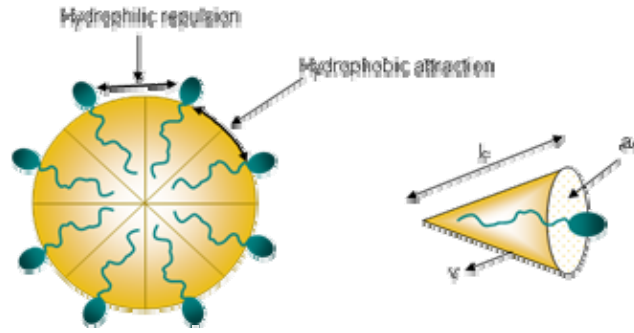
Figure 21: Schematic of aggregates formed by surfactants. Repulsive headgroup forces and attractive hydrophobic interfacial forces determine the optimum headgroup. The volume v and length l_c of the chain set limits on how the chains can pack together.
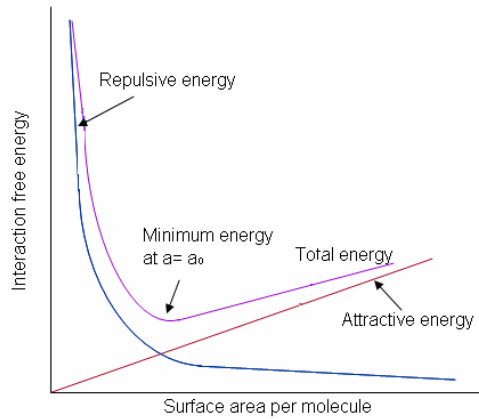
Figure 22: Optimal headgroup for which the opposing forces of the headgroup repulsion and interfacial attraction are balanced.

For a saturated hydrocarbon chain with n carbon atoms, Tanford (1973) determined that

$$l_c = 0.154 + 0.1265n \ \ (\text{nm}), \tag{3.55}$$

$$v = 27.4 + 26.9n \quad \text{(nm)} .\tag{3.56}$$

The shape of the surfactant aggregates depends on the critical packing shape, which is a function of the packing parameter. The different forms of the aggregates are illustrated in Table 4 [35].

One surfactant often used to form reverse micelles is sodium bis(2-ethylhexyl)sulfoccinate, commonly called AOT, which is represented as a truncated cone (Figure 23).
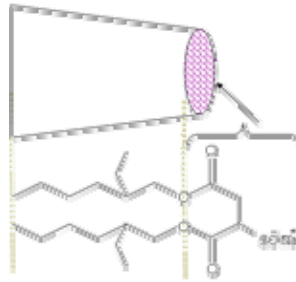
Figure 23: Shape of AOT surfactant forming reverse micelle

AOT is an anionic surfactant with two tails which can form reverse micelles with a great variety of solvents and without the need for a cosurfactant. AOT is characterized by a high degree of hydration (up to water/AOT ratio $w = 70$) and high molecular volume ($v = 600 \text{Å}^3$). The hydrocarbon chains have a length (l_c) of 8 Å and the area per polar head a_0 is of 60 Å^2 [36-38].
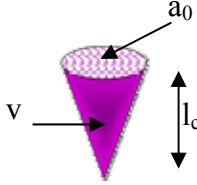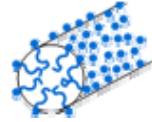
Close packing of AOT headgroups leaves an empty space in the center of the micellar core, which can be filled with water. Assuming that the volume and surface area of the micelles is governed by the water volume and by the surfactant, the water droplet radius can be expressed as

$$R = \frac{3V_{aq}[H_2O]}{a_0[AOT]},$$ (3.57)

where V_{aqu} is the volume per water molecule (30Å). Thus, the radius (in Å) of the water droplet is given by [39]

$$R = 1.5w.$$ (3.58)

Table 4: Packing shapes of surfactant and structure of their aggregates

Packing parameter	Critical packing shape	Structure formed
<1/3		
1/3-1/2		
1/2-1		
1		
>1		

Because the water droplet size is in the nano-scale, the droplets collide continuously due to Brownian motion. Hence a small fraction of droplets exist in the form of short-lived dimers which exchange their water content. After a short time, these dimers separate to form two droplets. As a result of this coalescence and separation mechanism, molecules solubilized in the water pools are redistributed over the micellar

population [39].   Taking advantage of this exchange process between droplets, reverse micelles have been used as nanoreactors for the synthesis of nanoparticles of different kinds of materials by coprecipitation or chemical reaction in the water droplets. The surfactant monolayer provides a barrier restricting the growth of the particles and hinders their coagulation. As a result, the particles possess a size similar to the water droplets [15, 34, 36, 39, 40].

Synthesis of nanoparticles by this method involves the preparation of two identical water-in-oil microemulsions (Figure 24), which only differ by the nature of their aqueous phase. One contains the metal salts (reactant A) and the other one the precipitating agent (reactant B).   Upon mixing, collisions and droplet coalescence bring the reactants A and B into contact to form the AB precipitate. This precipitate is confined to the interior of the reverse micelles and the size and shape of the particle formed ostensibly reflects the interior of the droplet [15].
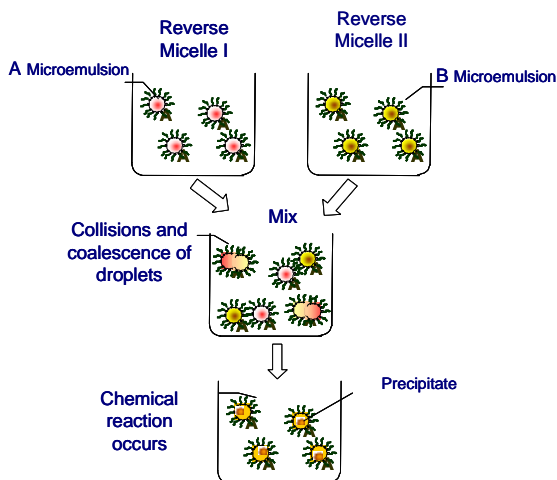
Figure 24: Schematic representation of nanoparticle synthesis using reverse micelles.

4. PREVIOUS WORK

Synthesis of nanoparticles with narrow diameter distribution has been a challenge for many researchers. Coprecipitation and templated synthesis using reverse micelles are two methods widely used for the synthesis of magnetic nanoparticles.

4.1. Coprecipitation

The coprecipitation method has been widely used to synthesize iron oxides. This method can produce particles with size ranging from a micrometer to nanometers, depending on the salts used. To obtain nanoparticles, Fe(II) and Fe(III) salts must be used whereas for particle sizes in the micrometer range only Fe(II) salt is necessary [31].

Fe_3O_4 nanoparticles were synthesized by Shen *et al* (1999) [41] using the coprecipitation method. Fe(II) and Fe(III) salts were chemically precipitated in the presence of decanoic acid and coated with n-alkanoic acids as a second surfactant. The particle size determined by TEM showed particles with mean diameter of 47 Å ($\ln \sigma_g = 13$) whereas magnetic measurements showed a diameter of 38 Å ($\ln \sigma_g = 11$). This difference in diameter was attributed to the formation of a non-magnetic layer on the surface of the nanoparticles [41]. Montagne *et al* (2002) [42] used iron (II) chloride tetrahydrate, iron (III) chloride hexahydrate, and ammonium hydroxide to synthesize Fe_3O_4 nanoparticles at room temperature. An Fe(III)/Fe(II) ratio of 2 was used in order to minimize the formation of non-magnetic hydroxides. The XRD pattern indicated formation of highly crystallized iron oxides with a calculated lattice constant of 8.36 Å, which is much closer to values corresponding to maghemite (8.35 Å) than to magnetite (8.40 Å). A diameter of 6.6 nm with a polydispersity index of 1.21 was determined.

Blaskov *et al* (1996) [43] obtained $CoFe_2O_4$ particles with a diameter of 50 ± 5Å by coprecipitation of Fe(II) and Co(II) solutions and calcination at 598 K for 6 h. Infrared spectroscopy showed bands at 458, 594, and 1098 cm^{-1}, close to bands characteristic of Fe-Co ferrites. Peaks in the XRD pattern corresponded to a cubic spinel lattice with a calculated value of 8.20 Å for the lattice parameter. The mean blocking temperature was

determined from the zero field cooled (ZFC) magnetization curve at a value of 250 K. The magnetization curve at 5 K showed hysteresis with coercivity of 14.5 kOe, reduced remanence (M_r/M_s) of 0.38, and saturation magnetization of 13 emu/g, which is lower than the saturation magnetization for the bulk material (93.9 emu/g at 5 K). The low reduced remanence was attributed to the fact that the particles did not saturate, the formation of agglomerates which may reduce the remanence, poor crystallinity, and incomplete occupation of magnetic ions in their respective sites.

4.2. *Templated synthesis using reverse micelles*

Reverse micelles have been used as an alternative method to synthesize nanoparticles. One of the systems most often used and studied is the combination water/AOT/isooctane.

Copper particles were synthesized using reverse micelles by Lisiecki *et al* (1993) [44]. The system water/AOT/isooctane and the reducing agent hydrazine were used. Copper clusters were obtained, confirming the controlled growth of the particles through reverse micelles. The particle size was controlled by the water/surfactant ratio (*w*), which was varied from 1 to 20. An increase in the particle size from 2 to 10 nm and low polydispersity were observed with increase of *w* from 1 to 10. For *w* greater than 10, a change in particle size was not observed. Electron diffraction showed a face-centered-cubic phase, and HRTEM showed an interreticular distance of 2 Å, which is in agreement with the value for the bulk phase.

Reverse micelles are believed to promote the synthesis of iron oxides at low reactant concentration and low temperature. This is because the micelles present a higher local concentration of Fe(II) in the Stern layer than homogeneous solutions and the oxygen solubility is also higher than in homogeneous solution, both of which favor the formation of $Fe(OH)_3$ and then Fe_3O_4 [31].

O'Connor *et al* (2001) [45] synthesized ferromagnetic metals and their alloys, ferrites, and magnetic alkaline fluoromanganates in this system. The ratio of

water/surfactant (w) was 7.5 and the precipitating agent was NH_4OH. Fe_3O_4, $CoFe_2O_4$, and $MnFe_2O_4$ were synthesized obtaining an average particle size of 5 nm which was determined by XRD and confirmed by TEM. Magnetic measurements were done at several fields. Blocking temperatures of 7 K (1000 G), 50 K (500 G) and 110 K (100 G) for Fe_3O_4 were observed whereas for $CoFe_2O_4$ they were 46 K (1000 G), 52 K(500 G) and 60 K (100 G). Values of coercivity and remanence of 500 G and 1.8 emu/g at 2 K were found for Fe_3O_4, while a coercivity of 6000 G and remanence of 2.2 emu/g were obtained for $CoFe_2O_4$. Metallic nanomaterials were synthesized in the system octane/cetyltrimethylammonium/water using as co-surfactant butanol (BuOH). A value of w=16 was used to synthesize Au/Fe/Au particles with diameter of 12 nm, 10 nm for $FePt_3$, and 18 nm for CoPt. $CoFe_2O_4$ was synthesized with 1, 1.5 and 2 Co/Fe ratios by Li *et al* (2001) [46]. AOT and isooctane were used to produce reverse micelles. Particle diameters in the range of 10 to 15 nm were obtained. Different values of the magnetic properties resulted for each Co/Fe ratio used in the synthesis. Blocking temperature measurements at 1000 G gave values of 45, 48, and 55 K and coercivity values at 10 K were 5870, 6430, and 7500 G for 1, 1.5, and 2 Co/Fe ratio, respectively.

Another surfactant often used to form reverse micelles is sodium dodecyl sulfate (SDS). Feltin *et al* (1997) [31] obtained Fe_3O_4 particles of 5.6 to 8.3 nm by varying the temperature from 25^oC to 80^oC. Sodium docecyl sulfate and ferrous chloride were used. XRD patterns showed low crystallininity for particles synthesized at temperatures less than 50^oC. At higher temperatures increased crystallinity was observed. XRD and Mossbauer spectra showed the formation of Fe_3O_4 only. This is in contrast with the coprecipitation method where the formation of maghemite is also observed [42]. TEM showed an increase in particle size with increasing temperature, obtaining 5.6 nm particles at 25^oC while at 80^oC the particle size was 8.3 nm. Magnetization curves showed remanence and coercivity only for particles with diameters of 8.3 nm. Moumen *et al* (1995) [47] used SDS to synthesize $CoFe_2O_4$ nanoparticles with 5 nm diameter. Elemental analysis showed that the particles are 65.63% iron and 34.37% cobalt. Magnetic measurements showed a coercivity of 8.8 kOe.

Pillai *et al* (1996) [15] used cetyl trimethyl ammonium bromide as the surfactant and a calcination process at 600°C to synthesize $CoFe_2O_4$ nanoparticles. Particles with diameter less than 50 nm were obtained. The measured saturation magnetization was 65 emu/g, remanence of 29 emu/g, and coercivity of 1440 Oe at 5 K.

4.3. *Magnetic anisotropy estimates*

One of the parameters due to which cobalt ferrites are of great interest is their high magnetocrystalline anisotropy constant. Different studies and methods have been used to determine this parameter yielding values in the order of 10^5-10^6 erg/cm^3. Rondinone *et al* (2000) [48] used superconducting quantum interference device (SQUID) magnetometry and Mossbauer spectroscopy techniques to determine the magnetic anisotropy constant (K) of 8.5 nm $CoFe_2O_4$ nanoparticles. Assuming the behaviour of superparamagnetic nanoparticles can be described by the Néel relaxation time (equation 1.54), an approximate value of K can be determined by obtaining the relaxation time at two different temperatures. Because SQUID and Mossbauer techniques use different measuring times, the ratio between the observed population with t greater than the measuring time and the unobserved population with t smaller has to be the same (50%). Considering this factor, a $\tau = 10$s at T=151 K was obtained from SQUID while $\tau = 10^{-8}$ s at T=394 K were obtained from Mossbauer measurements. Using equation 1.54, a K value of 2.23 x 10^6 erg/cm^3 was calculated. This value is in agreement with the value reported for the bulk material (1.8-3.0x10^6 erg/cm^3). Hanh *et al* (2003) used the AC susceptibility and Néel relaxation time to determine a value of $K = 5.36 \times 10^7$ erg/cm^3. Hyeon *et al* (2002) obtained a value of 5.5×10^6 erg/cm^3 for particles 6 nm diameter using the ZFC and FC curves and using the equation $K = 25kT/V$ for particles that are 4 nm diameter.

5. EXPERIMENTAL PROCEDURE

5.1. Materials.

Metal salts: Cobalt Chloride hexahydrate ($CoCl_2$ $6H_2O$, 98% pure from Fischer), and Ferrous Sulfate heptahydrate ($FeSO_4*7H_2O$, 99% pure from Fischer); Surfactant: Sodium Dioctyl Sulfosuccinate (AOT, 99 % pure from Fischer); Organic Solvent: Isobutyltrimethylmethane (Isooctane, 99% pure from Aldrich); methanol (CH_3OH, 99% pure from Aldrich). Dionized water (0.05 *uS/cm*) was obtained by treatment (Barnstead Nanopure Diamond).

5.2. Synthesis procedure.

Cobalt-substituted ferrite nanoparticles were synthesized using reverse micelles and 3:1, 4:1 and 5:1 Fe:Co ratios (Figure 22). For each Fe:Co ratio (3:1, 4:1, and 5:1) two reverse micelle precursor solutions were used. One contained both metal salts in the specified molar ratio and the other the ammonia solution. Reverse micelle solutions were prepared by adding a specific amount of aqueous solution to 0.5 M AOT in isooctane. In the case of the metal salt solution, the total concentration of metal ions was kept at 1 M. The metal ion solution was added to the AOT/isooctane solution in a 1:11 volume ratio in order to obtain a water to surfactant molar ratio of $w = 10$. The ammonia reverse micelle solution was prepared by adding 10% ammonia solution to the AOT/isooctane solution in a volume ratio of 1:8.

Magnetic nanoparticles were obtained by mixing under vigorous magnetic agitation equal volumes of the metal salt and ammonia reverse micelle solutions. The reaction was allowed to take place for 2 hours. Afterwards, the isooctane and water were removed by drying in a vacuum oven at 40ºC for 12 hours, leaving a dry dark residue of particles and surfactant. To remove the surfactant and excess ions, the residue was

washed several times using methanol, ethanol, and DI water successively, with each wash step followed by centrifugation. The final nanoparticle powder was obtained by drying the washed precipitate in a vacuum oven at 100ºC for 14 hours.

5.3. *Characterization.*

Characterization of the cobalt-ferrite nanoparticles was performed using the following techniques:

a. Transmission Electron Microscopy (TEM): The shape and size of the nanoparticles was determined using a Zeiss 922 200 kV TEM. Samples were prepared by placing a drop of cobalt ferrite microemulsion on a holey carbon-coated copper grid and dried with air at room temperature for several hours. The ImageJ program (distributed by NIH) was used to measure the diameter of the particles.

b. X-ray Diffraction (XRD): The structure and crystalline size of the nanoparticles was determined by XRD, using a Siemens D5000 diffractometer which is available in the General Engineering Department of the University of Puerto Rico Mayagüez. A scan rate of 0.008^{o}/s was used.

c. Superconducting Quantum Interference Device (SQUID): Magnetic properties of the nanoparticles, such as saturation magnetization, blocking temperature, coercivity, remanence, and initial permeability were measured in a Quantum Design MPMS XL-7 SQUID magnetometer equipped with an AC susceptometer. In order to eliminate the interaction of the particles in the samples, the powder was dispersed in paraffin.

d. Fourier Transform Infrared (FTIR): A Remspec mid-IR GAP interfaced to a Bruker Vector-22 spectrometer equipped with DTGS detector and a potassium bromide (KBr) beamsplitter was used to observe the characteristic bands of the metal-oxygen bonds in ferrites.

e. Elemental analysis: The amount of cobalt and iron present in the nanoparticles was determined by ICP-MS at Galbraith Laboratories, Inc.

6.   RESULTS

Elemental analyses are shown in Table 5. These analyses indicate an Fe:Co ratio is higher than expected for $CoFe_2O_4$ and consistently higher than that used in the synthesis. This implies that cobalt was not totally incorporated in the ferrite crystalline structure, hence a cobalt substituted ferrite $Co_xFe_{3-x}O_4$ was produced. The calculated x values are shown in Table 5. Using an Fe:Co ratio of 3:1, we obtain a cobalt substituted ferrite nearest to stoichiometric ferrite with a value of x of 0.61.

Table 6. ICP-MS analysis.

Preparation Fe:Co Ratio	Measured Fe:Co$_{exp}$ Ratio	x
3:1	3.9:1	0.61
4:1	5.8:1	0.44
5:1	6.4:1	0.41

FTIR spectra of the washed and dry samples indicated presence of AOT even after the wash process with ethanol and methanol. In order to eliminate the AOT of the cobalt substituted ferrites, the samples were washed again. In this case, isooctane was used to assure the dissolution of AOT. FTIR spectra were obtained for these samples (Figure 25) observing bands in ~1725cm^{-1}, ~1459 cm^{-1}, and ~1218 cm^{-1} which were attributed to shift bands of AOT. This shift (~10 cm^{-1}) is an indication of chemical bonding between AOT and the cobalt-substituted ferrite nanoparticles, therefore the wash process is not sufficient to eliminate the AOT from the nanoparticles. Bands at ~590cm^{-1} and ~400 cm^{-1} were also observed, which are characteristic of the metal-oxygen bonds of ferrites [49-52].
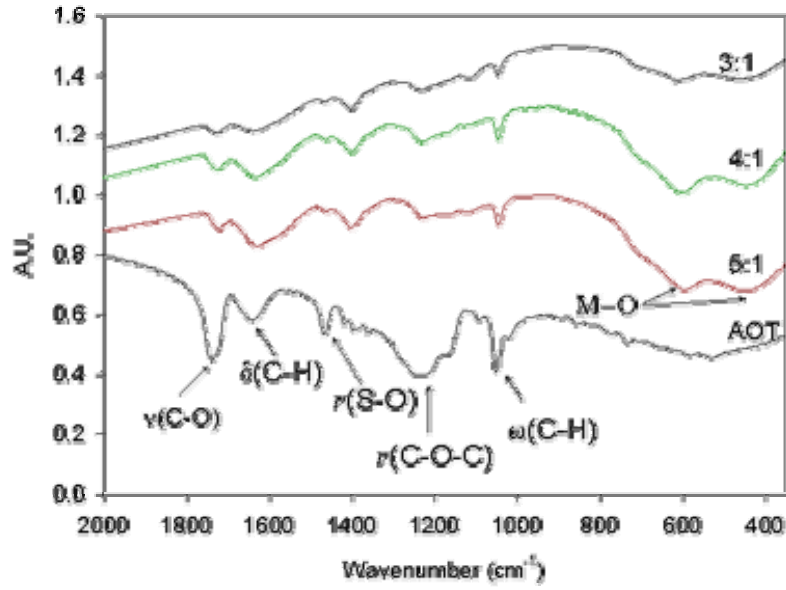
Figure 25: FTIR spectra of cobalt substituted ferrite (ν stretching, δ deformation, and ω wagging vibration).

X-ray diffraction of the powder, shown in Figure 26, confirms the formation of the FCC crystalline structure. The diffractogram for the sample synthesized with Fe:Co 3:1 presented a high background, because a faster scan rate (0.01°/s) was used. In order to improve the diffractogram a scan rate of 0.0008°/s was used for samples 4:1 and 5:1 Fe:Co. One can observe the peaks for the 311 and 511 planes typical of the inverse spinel of a ferrite. The background noise and presence of broad peaks are characteristic of particles with nanometer dimensions.

The mean crystallyte diameter was estimated using Scherrer's equation (6.1) and the 311 plane peak (Appendix A)

$$D \approx \frac{0.9\lambda}{\beta \cos\Theta},$$

(6.1)
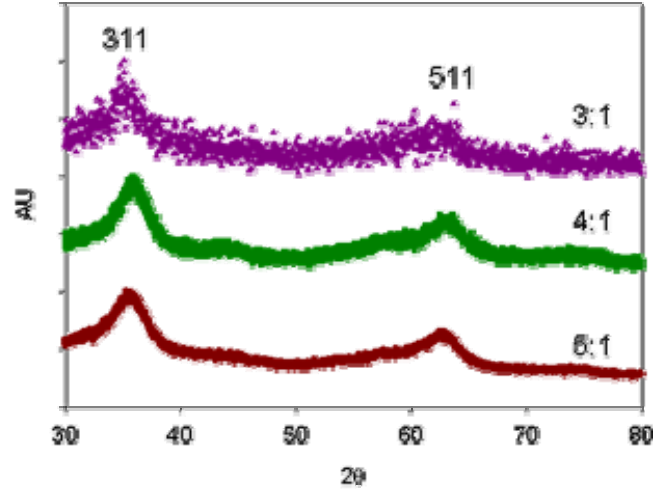
Figure 26: X-ray diffractogram of cobalt substituted ferrite. For sample 3:1 Fe:Co the scan rate was 0.01⁰/s whereas for samples 4:1 and 5:1 was 0.0008º/s .

where λ is the wavelength of the incident X-ray (1.54056 Å), θ is the diffraction angle, and β is the peak half-height width at θ. The interplane spacing d_{hkl} was determined using equation 6.2 and the lattice parameter a was determined by Bragg's law (equation 6.3)

$$d_{hkl} = \frac{\lambda}{2\sin\theta},$$

(6.2)

$$d_{hkl} = \frac{a}{\sqrt{h^2 + k^2 + l^2}}.$$

(6.3)

The values obtained are shown in Table 6. The lattice parameter a and interplanar spacing (d_{311}) for the $Co_{0.61}Fe_{2.39}O_4$ 3:1 sample are similar to values reported for bulk cobalt ferrite (a_0=8.39 Å and d_{hkl} = 2.52Å) [53, 54] whereas those for $Co_{0.44}Fe_{2.56}O_4$ (4:1) and $Co_{0.41}Fe_{2.59}O_4$ (5:1) are lower. The values obtained for sample 4:1 and 5:1 can be attributed to formation of another phase such as γ-Fe_2O_3.

Table 6: X-ray analysis. Lattice parameter (a), distance between 311 planes (d_{311}) and crystal diameter ($D_{X\text{-}ray}$).

Preparation Fe:Co Ratio	a (Å)	d_{311} (Å)	$D_{X\text{-}ray}$ (nm)
3:1	8.388	2.529	3.56
4:1	8.311	2.500	4.77
5:1	8.356	2.519	4.76
$CoFe_2O_4$[1]	8.394	2.531	
Fe_3O_4[2]	8.398	2.532	
$\gamma\text{-}Fe_2O_3$[3]	8.347	2.517	

[1] Ref. [55]
[2] Ref. [56]
[3] Ref. [57]

A TEM image of $Co_{0.61}Fe_{2.39}O_4$ (3:1) is shown in Figure 27. TEM images for cobalt substituted ferrites 4:1 and 5:1 are shown in Appendix B. The particles seem spherical as expected. The particle size distribution was determined from diameter measurements of 350 nanoparticles and a regression giving a good fit with a lognormal distribution (Figure 28). The median diameter and standard deviation (Appendix B) for the samples synthesized are shown in Table 7.
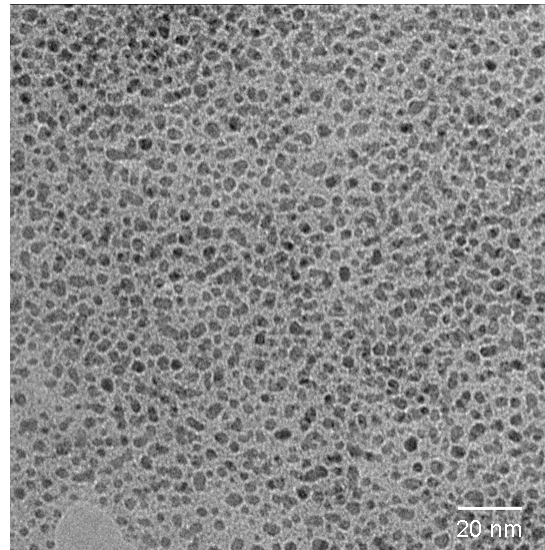
Figure 27: TEM image of cobalt substituted ferrite synthesize with a 3:1 Fe:Co ratio.
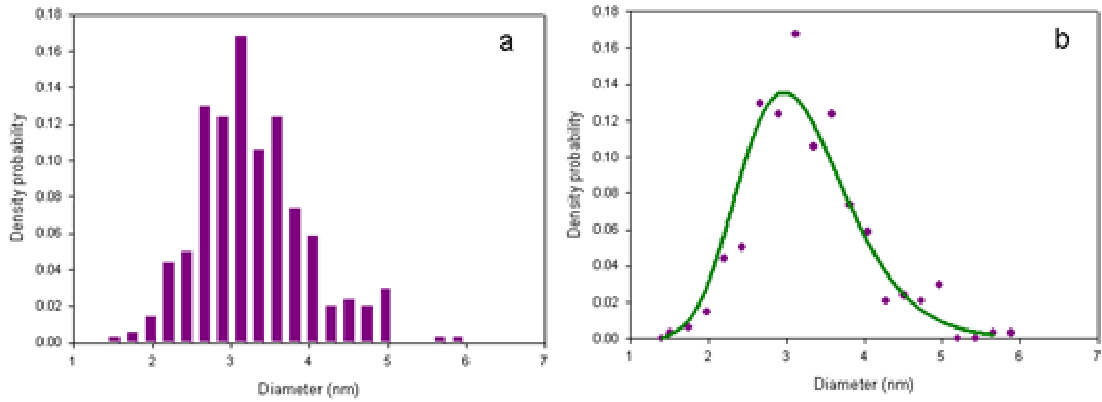
Figure 28: Diameter distribution measured in TEM for cobalt substituted ferrite 3:1 Fe:Co ratio. (a) Histogram and (b) lognormal distribution.

Magnetization curves were obtained at 5 and 300 K with applied fields of up to 50 kOe (5 Tesla). Figure 29 shows results for the three samples synthesized. In all cases, the magnetization curve at 5K shows hysteresis with coercivity higher that 8 kOe (~0.8 T, Table 8), which is characteristic of single domain particles. Similar results were observed for cobalt ferrite nanoparticles by Ahn *et al* (2001)[58], Song *et al* (2004) [59], Ammar *et al* (2001) [60], and Tung *et al* (2003) [16].

Table 7: Particle diameter and standard deviation determined from TEM images.

Preparation Fe:Co Ratio	D_{pg} (nm)	$Ln\ \sigma_g$	D_{pgv} (nm)
3:1	3.20	0.21	3.66
4:1	3.44	0.12	3.60
5:1	3.04	0.18	3.34

For the sample with 4:1 Fe:Co ratio, the magnetization curve at 5 K shows a short step change in the magnetization at low fields. Similar results were observed by Ammar *et al* (2001) [60], which attributed this step change to particle-particle interactions when the powder samples were not well dispersed. Figure 30 shows the magnetization curves of the cobalt substituted particles without dispersion in wax, confirming the observations done by Ammar *et al* (2001) [60].
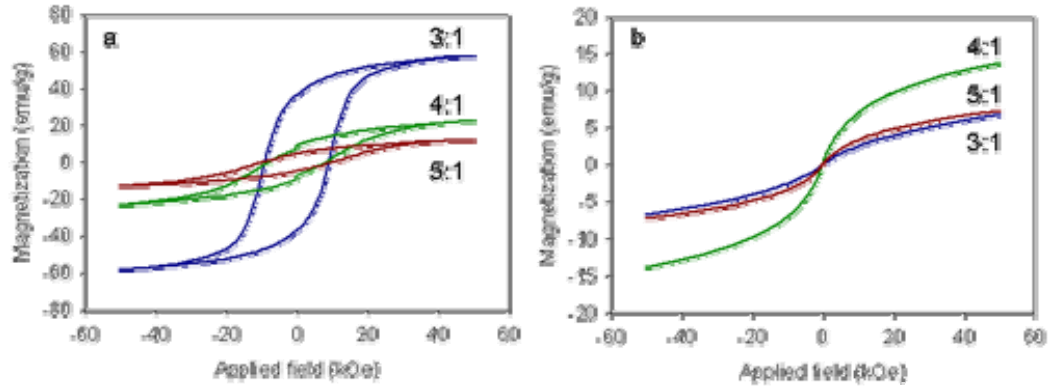
Figure 29: Magnetization curve for cobalt substituted ferrite dispersed in wax at (a) 5 K and (b) 300 K.

Table 8: Magnetic properties of cobalt substituted ferrites.

Fe:Co Ratio	M_r (5 K) (emu/g)	H_c (5 K) (kOe)	χ_0(T-To)	T_0 (K)
3:1	36.40	9.08	0.418	53.14
4:1	7.60	8.05	1.542	71.41
5:1	4.56	9.94	0.781	83.34

In order to determine the dependence of χ_0 with temperature, magnetization measurements at low fields and different temperatures were made for the three samples (Appendix C). Figure 31a shows linear behavior between magnetization and applied field, with slope χ_0. Figure 31b shows the expected temperature dependence from equation (3.50) for a system of interacting particles. The values for T_0 and $\chi_0(T - T_0)$ are shown in Table 8. High values of T_0 ($T_0>50K$) were obtained despite the fact that the samples were dispersed in paraffin; therefore the interparticle interaction must be considered in the analysis.
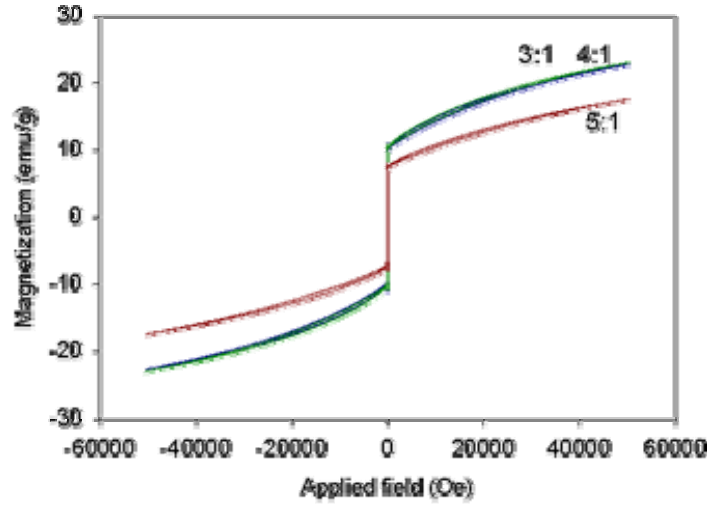
Figure 30: Magnetization curve for cobalt substituted ferrite powder at 5 K.
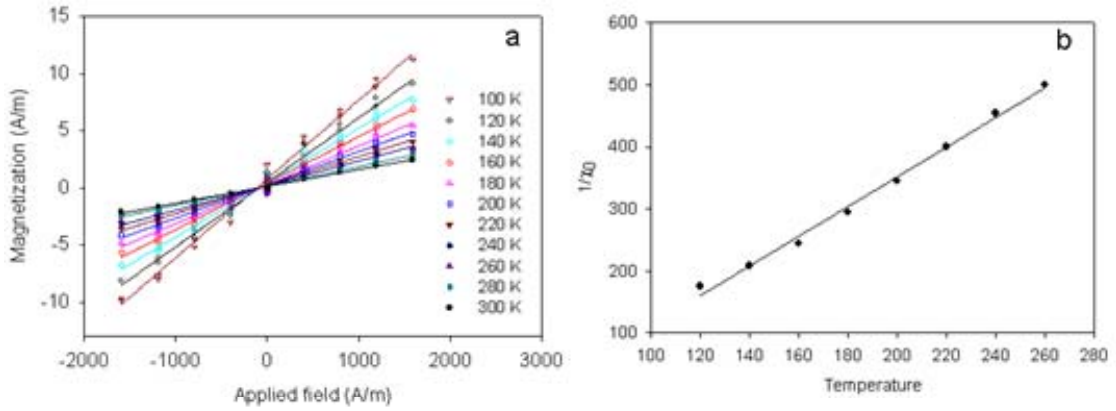
Figure 31: (a) Magnetization curve at low field (300 K) and (b) relation between χ_0 and temperature for cobalt substituted ferrite 3:1.

The volume median particle diameter was determined using equation (3.38) (illustrated in Table 7). Considering $\overline{D}_{pgv}$, equation (1.51) and the curves at 300 K, the domain magnetization and volume fraction were determined (Appendix D).

In order to calculate the domain magnetization, the saturation magnetization and χ_0 must be determined. The saturation magnetization was calculated from the intercept of the magnetization curve at high field (Figure 32a) whereas χ_0 was determined using the slope of the magnetization curve at low field (Figure 32b). Sample calculations are presented in Appendix D, and values of M_s, χ_0, M_d, and ϕ are illustrated in Table 9.

54
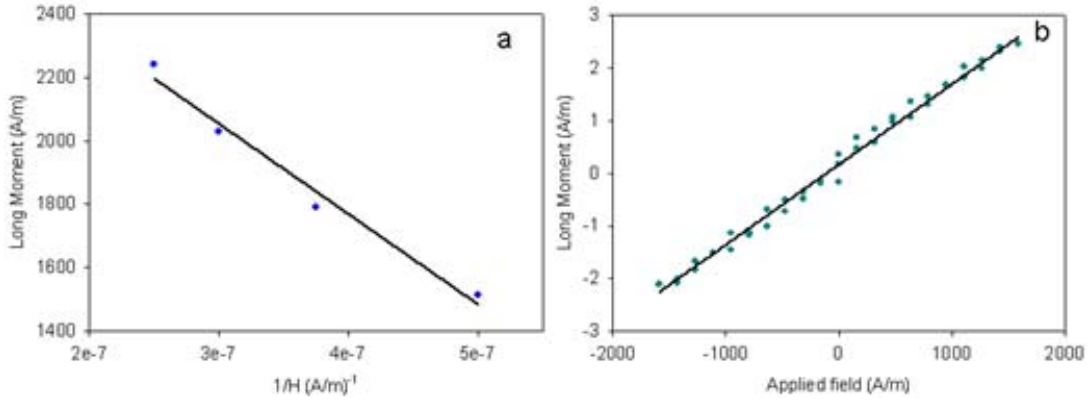
Figure 32: Magnetization curve (300K) at (a) high field and (b) low field for the cobalt substituted ferrite 3:1.

Table 9: Magnetic properties of cobalt substituted ferrite.

Fe:Co Ratio	M_s (300 K) (emu/g)	M_s (5 K) (emu/g)	M_r/M_s 5K	χ_0	M_d (300K) (emu/g)	ϕ
3:1	8.83	62.02	0.587	0.0015	41.31	0.21
4:1	12.40	26.57	0.286	0.0067	121.73	0.10
5:1	6.44	15.22	0.300	0.0042	121.93	0.05
$CoFe_2O_4$	80.3	90.8	0.83 (0K)		80.3	
Fe_3O_4	85.7				85.7	
$\gamma\text{-}Fe_2O_3$	72.0[1]				72.0[1]	

[1] Ref. [61]

The saturation magnetization value calculated for samples synthesized using reverse micelles is less than reported in the literature. Tung *et al* (2003) obtained a saturation magnetization value of 67.95 emu/g at 300 K and 94 emu/g at 5 K for particles of 3.3 nm magnetic diameter [16]. Ammar *et al* [60] observed values of 85.1 emu/g at 5 K and 65 emu/g at 300 K for saturation magnetization of cobalt ferrite. Hanh *et al* [62] observed a M_s = 75 emu/g at 5 K for cobalt substituted ferrite with a Fe/Co ratio of 1.85.

Our low value of saturation magnetization can be attributed to particles not saturating (illustrated in Figure 29), hence the value calculated of M_s is underestimated. The sample synthesized with a ratio 4:1 presents M_s higher than sample 3:1,which can be due to its larger particle size (~1 nm greater) and lower cobalt content. The formation of a mixture of ferrites can also be hypothesized as a cause of the difference of M_s. In the case of sample 4:1 we can consider a mixture of cobalt ferrite and magnetite whereas in sample 5:1 a mixture of cobalt ferrite and maghemite based on the M_s for maghemite (~72 emu/g) being less than magnetite (~85.72 emu/g). This hypothesis can also explain the low values of domain magnetization found for the samples. Although the presence of AOT on the surface [53] of the particles and use of the diameter estimated by TEM in equation (1.50) can also cause low values for M_d.

The synthesized magnetic nanoparticles synthesized present a reduced remanent magnetization (M_r/M_s at 5 K) lower than that for cubic positive anisotropy at 0 K (0.83) [16] as is the case of $CoFe_2O_4$ (bulk). For $Co_{0.61}Fe_{2.39}O_4$ (3:1) M_r/M_s was 0.587, a value near that for non-interacting uniaxial single-domain particles. Tung *et al* [16] obtained a value of M_r/M_s = 0.46 at 2 K for 3.3 nm magnetic diameter particles. Similar results were observed by Moumen *et al* [17] with a value of 0.43 for particles with 3 nm diameter. For cobalt-substituted ferrite (65.63% iron and 34.37% Co) of 5 nm diameter, Moumen *et al* [47] found a value of 0.74 to M_r/M_s at 20 K. Ammar *et al* [60] observed a reduced remanence magnetization value of 0.67 for particles of 5 nm diameter. A similar value (0.65 at 5 K) was obtained by Hanh *et al* [62].

Zero field cooled (ZFC) and field cooled (FC) magnetization curves were obtained for each sample at 100 Oe (Figure 33). Zero field cooled curves were obtained by cooling the sample under zero applied field to 5 K, then applying the desired field and slowly warming the sample to 300 K. Field cooled curves were obtained by cooling the sample from 300 K to 5 K under the applied field. Phenomenologically, the peak of the ZFC curve corresponds to a state where the particles cross over from superparamagnetic behavior to ferromagnetic behavior with decreasing temperature. The temperature at

which this peak occurs is commonly referred to as the blocking temperature (Table 10). Li, *et al* [63] reported blocking temperatures of 45 and 65 K under an applied field of 1000 Oe for 3:1 and 5:1 Fe:Co ratios respectively and blocking temperature in the range from 45 to 55 K for different compositions [46] which are lower than our observed temperatures of 60.8 K and 79 K. Seip *et al* [64] observed that at 100 and 1000 Oe blocking temperatures are similar (46 K and 52 K respectively) for cobalt ferrite whereas for magnetite they vary considerably (7 and 50 K respectively).
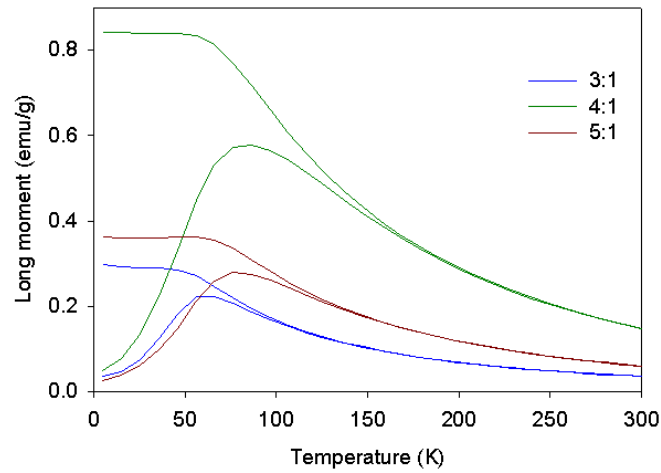
Figure 33: Field cooled and zero field cooled magnetization as a function of temperature for cobalt substituted ferrites dispersed in wax under an applied field of 100 Oe.

Comparing the values obtained of blocking temperature and particle diameter, we observe that the highest blocking temperature corresponds to the largest size particle whereas the lowest blocking temperature corresponds to the smallest particle size particles.

Table 10:Blocking temperature.

Fe:Co Ratio	T_B (K) 100 Oe
3:1	60.8
4:1	83.4
5:1	79.0

The in-phase component of the magnetic susceptibility χ' was measured as a function of temperature for various frequencies. As seen in Figure 34, the in-phase component of the AC susceptibility displays a peak with respect to temperature. The variation of this peak with applied frequency can be used to estimate the magnetic anisotropy (similar curve for samples 4:1 and 5:1 are shown in Appendix E). According to the Debye model for dipolar systems [65], the in-phase component of the AC susceptibility χ' is given by

$$\chi' = \frac{\chi_0}{1 + \tau^2 \Omega^2}, \tag{6.4}$$

where χ_0 and τ are functions of temperature, τ is the magnetic relaxation time, and Ω is the applied field frequency. Because the small-amplitude AC field represents a small departure from equilibrium, we assume the low-field limit of the Langevin equation applies and χ_0 is given by Equation (2-31). We further assume magnetic relaxation occurs by the Néel process, hence the characteristic relaxation time is given by equation (1-54).

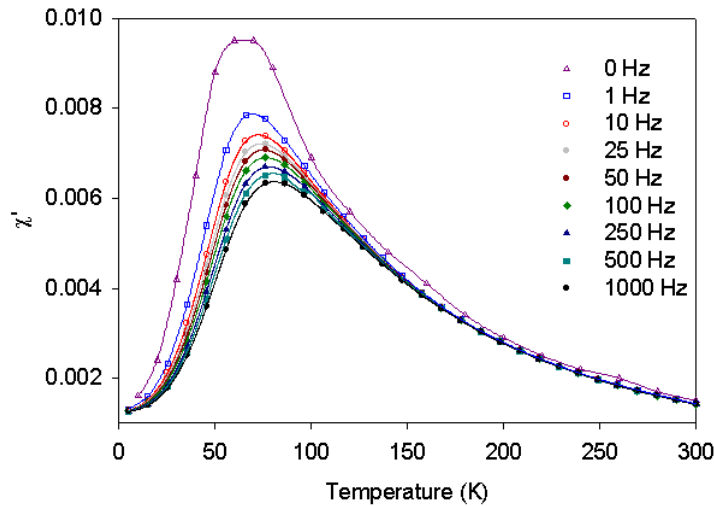

Figure 34: In-phase component of the AC susceptibility χ' as a function of temperature for various frequencies in the cobalt substituted ferrite prepared with Fe:Co ratio of 3:1 and dispersed in wax. Solid lines are guides for the reader.

Arguably the Debye model of equation (6.4) may seem simplistic or naive, however we note that the results of a rigorous analysis by Raikher and Stepanov [66] reduce to this equation for the limits

$$\Omega\tau_D << 1 \; ; \; \Omega^2\tau^2 << KV/kT \; ; \; KV/kT >> 1 \tag{6.5}$$

where $\tau_D = \dfrac{KV}{kT}\tau_0$. The first condition is easily met for the frequencies considered here, whereas the final condition may be easily checked after obtaining values for K from analyzing the experimental measurements.

Taking the derivative of equation (6.4) with respect to temperature results in

$$\frac{1}{1+\Omega^2\tau^2}\frac{\partial\chi_0}{\partial T} - \frac{2\tau\Omega^2}{(1+\Omega^2\tau^2)^2}\chi_0\frac{\partial\tau}{\partial T} = 0 \;. \tag{6.6}$$

Assuming negligible interparticle interaction we have

$$\frac{\partial\chi_0}{\partial T} = -\frac{\pi\phi\mu_0 M_d^3 D^3}{18kT^2} = \frac{-\chi_0}{T} \;, \tag{6.7}$$

and

$$\frac{\partial\tau}{\partial T} = -\frac{KV}{kT^2}\tau_0\exp\left(\frac{KV}{kT}\right) = -\frac{KV}{kT^2}\tau \;. \tag{6.8}$$

replacing equations (6.7) and (6.8) in equation (6.6) and collecting terms (Appendix F) gives

$$\tau^2\Omega^2 = \frac{\chi_0 kT}{2\chi' KV} \;, \tag{6.9}$$

$$\frac{1}{T_{max}} = \frac{18k}{\pi\phi\mu_0 M_d^2 D^3}\chi'_{max} + \frac{k}{2KV} \;, \tag{6.10}$$

59

where T_{max} is the temperature corresponding to the peak of the in-phase component of the AC susceptibility, for which $\chi' = \chi'_{max}$. Equation (6.10) is linear with slope $\dfrac{18k}{\pi\phi\mu_0 M_d^2 D^3}$ and intercept $\dfrac{k}{2KV}$, when $1/T_{max}$ is plotted against χ'_{max}.

If the interparticle interaction is included in the analysis, equation (3.50) and (6.7) are substituted in equation (6.6) resulting in

$$\frac{\partial \chi_0}{\partial T} = -\frac{\pi\phi\mu_0 M_d^3 D^3}{18k(T-T_0)^2} = \frac{-\chi_0}{(T-T_0)}, \tag{6.11}$$

$$\Omega^2 \tau^2 = \frac{1}{\dfrac{2KV(T-T_0)}{kT^2} - 1} \textbf{Error! Reference source not found.} \tag{6.12}$$

$$\frac{T_{max}^2}{T_{max}-T_0} = \frac{2KV}{k} - \frac{36KV}{\pi\phi\mu_0 M_d^2 D^3}(T_{max}-T_0)\chi'_{max}. \tag{6.13}$$

Equation (6.13) is linear with slope $\dfrac{36KV}{\pi\phi\mu_0 M_d^2 D^3}$ and intercept $\dfrac{2KV}{k}$, when $\dfrac{T_{max}^2}{T_{max}-T_0}$ is plotted against $(T_{max}-T_0)\chi'_{max}$.

The curves described by equations (6.10) and (6.13) are shown in Figure 35 for the sample synthesized with an Fe:Co ratio of 3:1.

Commonly it is assumed that the peak of the χ' vs. T curve corresponds to the condition $\Omega\tau = 1$, hence plotting $\ln(1/\Omega)$ vs. $1/T$ should yield a linear relation in which the slope provides an estimate for KV (equation 6.14). Figure 36 shows the data analized using this assumption.

$$\ln\frac{1}{\Omega} = \ln\tau_0 + \frac{KV}{kT} \qquad (6.14)$$
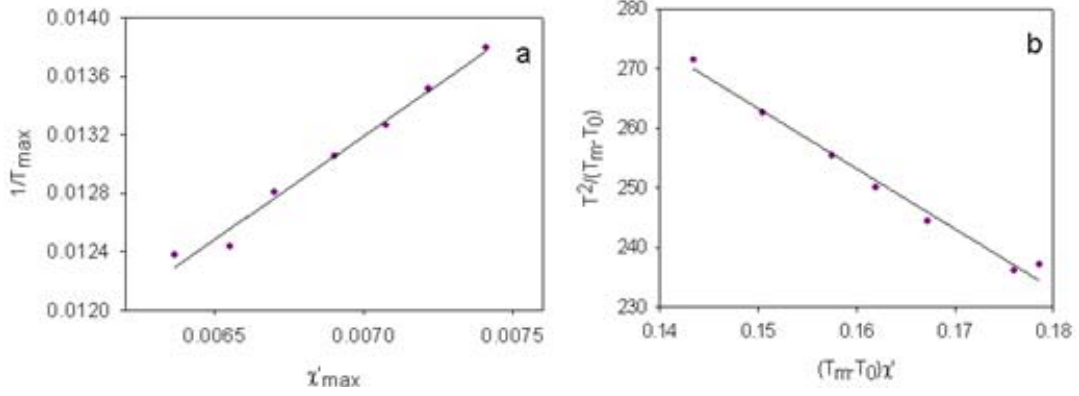
Figure 35: Relation between the in-phase component of the AC susceptibility χ' and temperature corresponding to the maximum T_{max} for the cobalt substituted ferrite prepared with Fe:Co ratio of 3:1 considering (a) negligible interparticle interaction and (b) interparticle interaction.

Using $\overline{D}_{pgv}$ to calculate the particle volume, the anisotropy constant was calculated using equations (6.10), (6.13), and (6.14). The results are presented in Table 11.
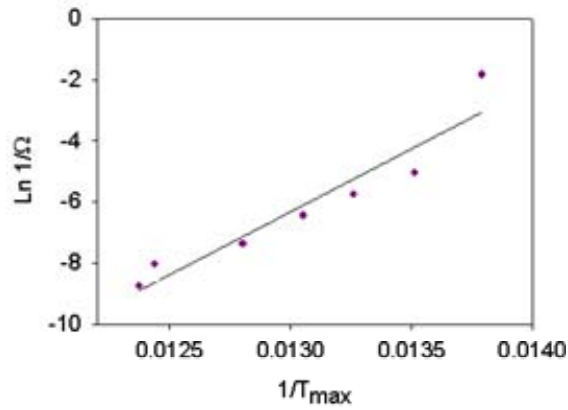
Figure 36: Relation between the inverse applied field frequency $1/\Omega_f$ and the inverse temperature Tmax corresponding to a maximum in χ'.

Table 11: Anisotropy constants: K_{To} assuming interparticle interaction, K assuming negligible interparticle interaction, and $K_{Néel}$ assuming $\Omega\tau = 1$.

Fe:Co Ratio	K_{T0} (kerg/cm^3)	K (kerg/cm^3)	$K_{Néel}$ (kerg/cm^3)
3:1	1118.2	816.4	22197.9
4:1	1681.0	882.9	25837.7
5:1	4684.2	1072.2	31058.8

Our values for the magnetic anisotropy constant (K_{T0}) differ considerably from values reported for similarly synthesized cobalt ferrite particles. For example, Hsieh and Lue [67] report values that are two orders of magnitude larger, whereas Tung *et al.* [16] and Hanh *et al.* [62] report values that are three orders of magnitude larger. We attribute the difference to a discrepancy in the way in which the AC susceptibility measurements have been analyzed. Commonly it is assumed that the peak of the χ' vs. T curve corresponds to the condition $\Omega\tau = 1$, which we have disproved with our analysis using the Debye model for the in-phase component of susceptibility (Equation 6.4). $\Omega\tau$ takes the value of 1 in the peak of the out-phase component of the susceptibility change with frequency curve (Appendix F). The condition $\Omega\tau = 1$ also applies for the peak of χ' vs. T when τ corresponds to a Brownian relaxation time (Appendix F) [68]. If we calculate the anisotropy constant assuming $\Omega\tau = 1$, $K_{Néel}$ (Table 11), the values obtained are similar to those reported in the literature. Ammar *et al* [60] report a value of 1.6×10^7 erg/cm^3 and Hanh *et al* [62] observed a value of 5.36×10^7 erg/cm^3.

7. CONCLUSIONS

Cobalt-substituted ferrite nanoparticles with FCC structure have been synthesized using reverse micelles. Because the reverse micelles act as templates, we obtained nanoparticles with approximately 3 nm diameter and narrow size distribution. Despite the advantages posed by the reverse micelles, the method produces particles that are chemically bound to AOT, which is difficult to eliminate with a wash process. The presence of AOT in the nanoparticles can be inconvenient when the particles must be funtionalized with biomolecules, for use in a biosensor. Magnetic measurements show interparticle interaction despite dispersing the particles in paraffin. Superparamagnetic behavior was observed at 300 K whereas ferrimagnetic behavior was observed at 5 K. The ferrimagnetic behavior of the cobalt-substituted ferrite is characterized by coercivity values higher than 8 kOe, characteristic of cobalt ferrite nanoparticles. A Debye model provides a new alternative to determine the anisotropy constant using AC susceptibility measurements. Anisotropy values in the order of $\sim 10^6$ erg/cm^3 (in agreement with the bulk value) were obtained whereas values of $\sim 10^7$ erg/cm^3 were obtained assuming $\Omega\tau = 1$, as is typically done in the literature. A rigorous analysis was used to determine the temperature dependence of the peak of the in-phase component of the AC susceptibility curve when the relaxation time corresponds to a Néel process. This analysis demonstrates that the assumption that $\Omega\tau = 1$ at the peak of the in-phase AC susceptibility with respect to temperature is not rigorously valid.

8. RECOMMENDATIONS

In this work, we have obtained cobalt-substituted ferrite nanoparticles using reverse micelles at room temperature. A study at different temperatures could be done in order to determine the influence of temperature on cobalt ferrite formation and how this affects the value of the anisotropy constant.

The co-precipitation method could be used to synthesize cobalt ferrite nanoparticles at temperatures higher than room temperature. A comparison between nanoparticles synthesized by co-precipitation and reverse micelles may be done in order to determine if there are changes in the properties of cobalt ferrite particles and to study the effect of the binding of AOT to the nanoparticle surface.

Because binding of AOT to the nanoparticle surface is inconvenient for functionalization for sensor applications, a method to eliminate or replace the AOT should be developed.

APPENDIX A

Determination of particle diameter using Scherrer's equation
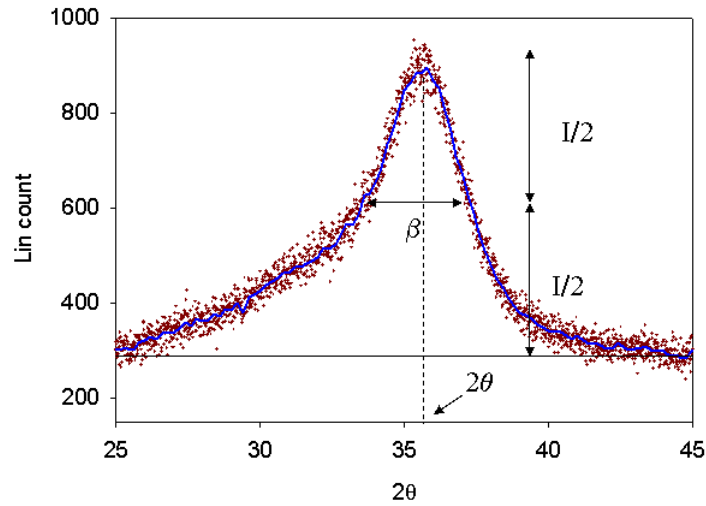
Figure 37: X-ray diffractogram for sample 5:1 Fe:Co in the 2θ range of 25 - 45° corresponding to the 311 plane.

Considering Figure 37, we obtained the following values for the parameters in Scherrer's equation:

$$2\theta = 35.6^o$$

$$\beta(radians) = \frac{3.5^o \times \pi}{180} = 0.061087$$

Substituting in equations 6.1 to 6.3 we obtain

$$d(nm) = \frac{0.9(1.54056)}{0.061087\cos\left(\frac{35.6}{2}\right)} = 4.76nm$$

$$d_{hkl} = \frac{1.54056}{2\sin\left(\dfrac{35.6}{2}\right)} = 2.5197 \text{ Å}$$

$$a = 2.5197\sqrt{3^2 + 1^2 + 1^2} = 8.3568 \text{ Å}$$

APPENDIX B

TEM images for cobalt substituted ferrites synthesized using reverse micelles.
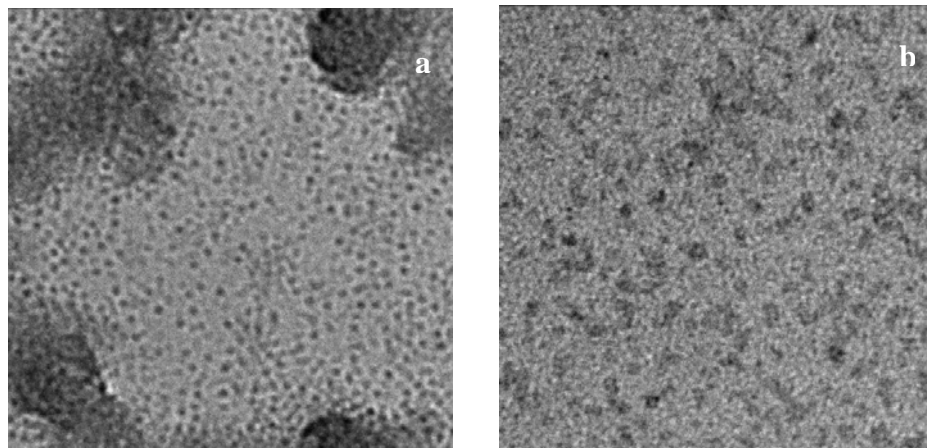
Figure 38: TEM image of (a) $Co_{0.44}Fe_{0.56}O_4$ (4:1) nanoparticles and (b) $Co_{0.41}Fe_{0.59}O_4$ (5:1) nanoparticles.
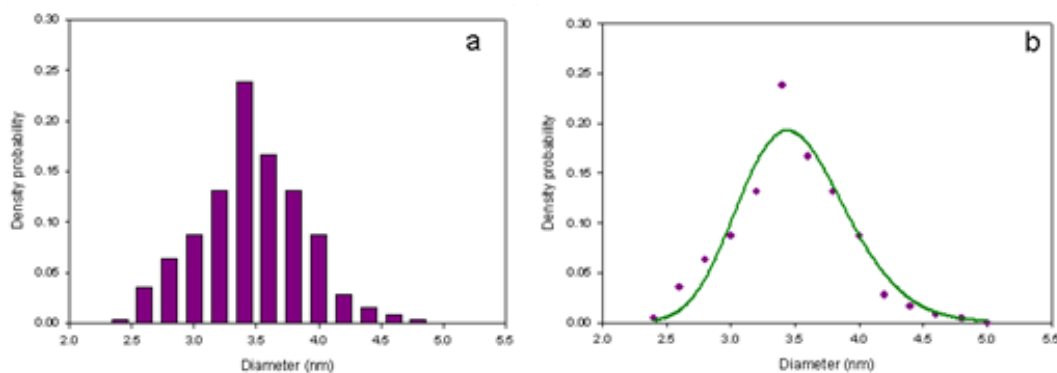
Figure 39: Statistical analysis of diameter measured in TEM image of cobalt substituted ferrite 4:1 Fe:Co ratio (a) Histrogram and (b) lognormal distribution.
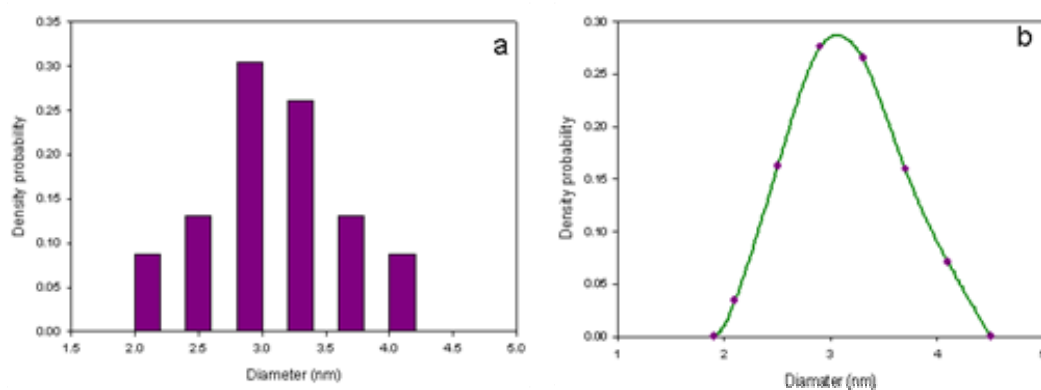
Figure *40: Statistical analysis of diameter measured in TEM image of cobalt substituted ferrite 5:1 Fe:Co ratio (a) Histrogram and (b) lognormal distribution.*

APPENDIX C

Relation between χ_0 and temperature for cobalt substituted ferrite nanoparticles.
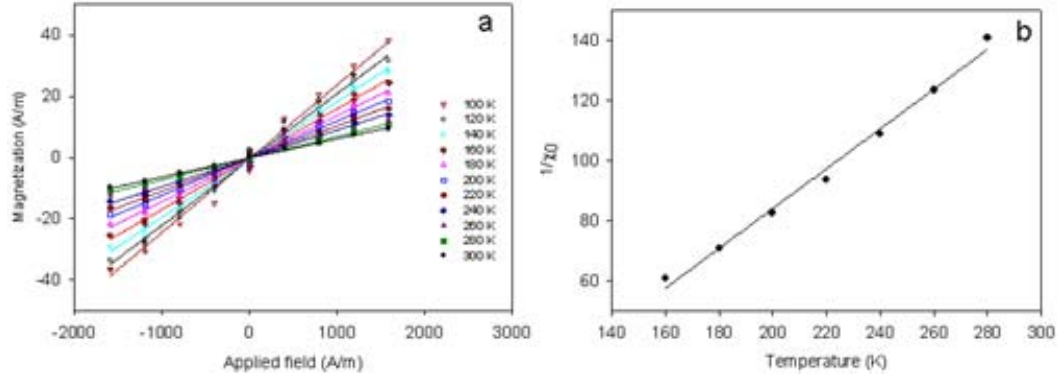
Figure 41: (a) Magnetization curve at low field (300 K) and (b) relation between χ_0 and temperature for cobalt substituted ferrite 4:1.
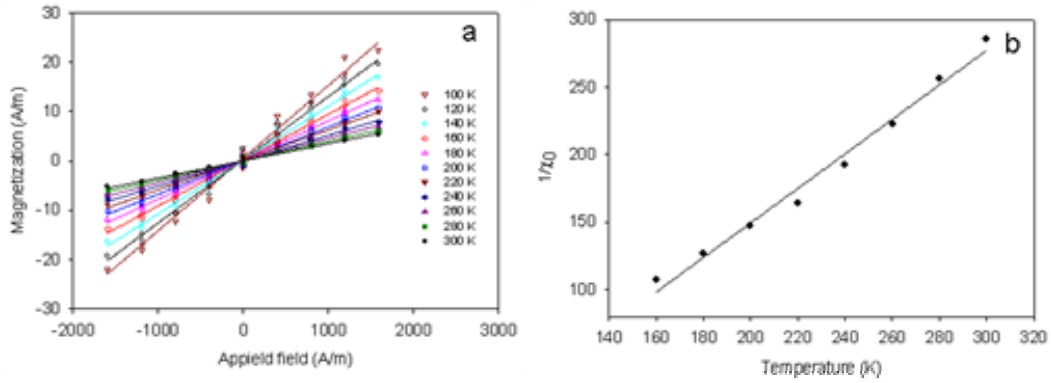
Figure 42: (a) Magnetization curve at low field (300 K) and (b) relation between χ_0 and temperature for cobalt substituted ferrite 5:1.

APPENDIX D

Determination of domain magnetization and volume fraction

Considering the Langevin equation at high field, equation (3.33) is obtained. Performing a linear regression at high field (Figure 43), the magnetic behavior can be described by equation (D-1) for the sample 4:1. When $1/H = 0$, the magnetization value is the saturation magnetization (M_s). For the sample 4:1 M_s= 14641.92 A/m.
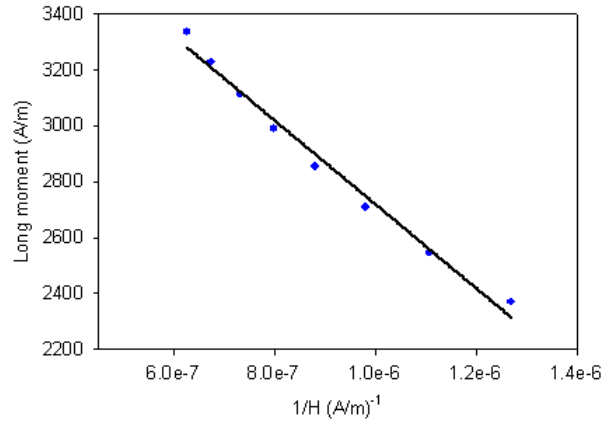
Figure 43: *Magnetization at high fields (300K) for cobalt substituted ferrite 4:1.*

$$M = \frac{-5.207 \times 10^9}{H} + 14641.92 \qquad \text{(D.1)}$$

Considering the Langevin equation at low field, equation (3.31) is obtained. Performing a linear regression at low field (Figure 44), the magnetic behavior can be described by equation (D-2) for the sample 4:1 with a value of $\chi_0 = 0.0067$.

$$M = 0.0067H + 0.3289 \qquad \text{(D.2)}$$
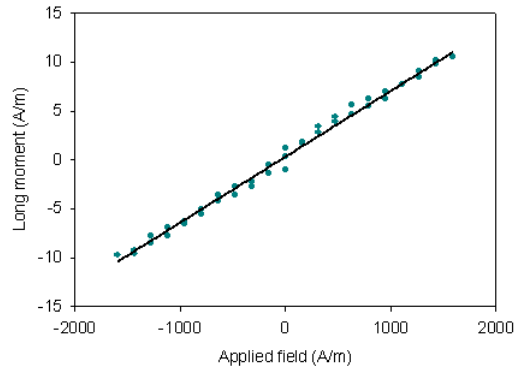
Figure 44: Magnetization at low fields (300K) for cobalt substituted ferrite 4:1.

Using equation (3.48), we obtain the following expression for the domain magnetization

$$M_d = \frac{18k}{\pi\mu_0 \overline{D}_{pgv}^3} \sqrt{\frac{\chi_0 T(T-T_0)}{3M_s H_0}} \; .$$

For the sample 4:1 with $T_0 = 71.41K$, $M_s = 4219.82\text{A/m}$, $\chi_0 = 0.0067$, and $\overline{D}_{pgv} = 3.6\text{nm}$ we obtain $M_d = 430927.6$ A/m. The volume fraction is then calculated from $\phi = M_s / M_d$

APPENDIX E

In-phase component of the AC susceptibility χ'
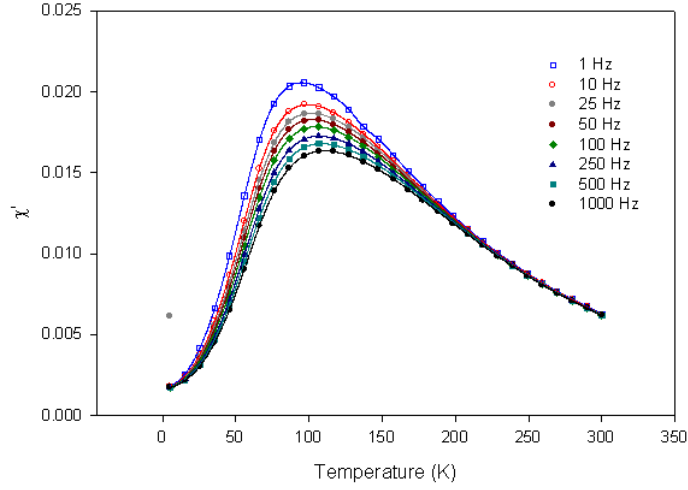
Figure 45: In-phase component of the AC susceptibility χ' as a function of temperature for various frequencies in the cobalt substituted ferrite prepared with Fe:Co ratio of 4:1 and dispersed in wax
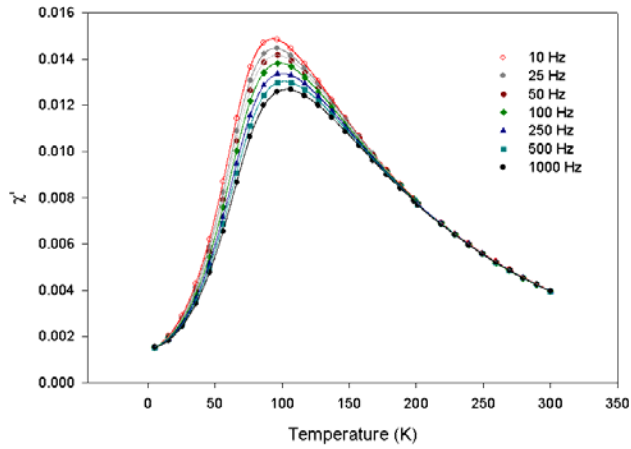
Figure 46: In-phase component of the AC susceptibility χ' as a fuction of temperature for various frequencies in the cobalt substituted ferrite prepared with Fe:Co ratio of 5:1 and dispersed in wax

71

APPENDIX F

An equation to determine the anisotropy constant through the in-phase component of AC susceptibility χ'

Take the derivate of χ' with T to obtain

$$\frac{1}{1+\Omega^2\tau^2}\frac{\partial\chi_0}{\partial T} - \frac{2\tau\Omega^2}{(1+\Omega^2\tau^2)^2}\chi_0\frac{\partial\tau}{\partial T} = 0 \qquad \text{(E-1)}$$

where

$$\frac{\partial\tau}{\partial T} = -\frac{KV}{kT^2}\tau_0\exp\left(\frac{KV}{kT}\right) = -\frac{KV}{kT^2}\tau \qquad \text{(E-2)}$$

a. *Considering negligible interparticle interaction*

$$\frac{\partial\chi_0}{\partial T} = -\frac{\pi\phi\mu_0 M_d^3 D^3}{18kT^2} = \frac{-\chi_0}{T} \qquad \text{(E-3)}$$

Replacing (E-2) and (E-3) in (E-1) gives

$$-\chi_0 kT + 2\tau^2\Omega^2\chi'KV = 0$$

grouping terms

$$\tau^2\Omega^2 = \frac{\chi_0 kT}{2\chi'KV} \qquad \text{(E-4)}$$

$$\Omega^2\tau^2 = \frac{1}{\dfrac{2KV}{kT}-1}$$

from the Debye model

$$\Omega^2 \tau^2 = \frac{\chi_0 - \chi'}{\chi'} \tag{E-5}$$

equating (E-4) and (E-5) and taking the reciprocal yields

$$\frac{\chi'}{\chi_0 - \chi'} = \frac{2\chi' KV}{\chi_0 kT} \tag{E-6}$$

accommodating terms

$$(2KV - kT)\chi_0 = 2KV \chi' \tag{E-7}$$

replacing the value of χ_0 (equation 3.46)

$$\frac{\pi \phi \mu_0 M_d^2 D^3}{18} \left(\frac{2KV}{KT} - 1 \right) = 2KV \chi' \tag{E-8}$$

accommodating terms

$$\frac{1}{T_{max}} = \frac{18k}{\pi \phi \mu_0 M_d^2 D^3} \chi' + \frac{k}{2KV} \tag{E-9}$$

b. *Considering interparticle interaction*

$$\frac{\partial \chi_0}{\partial T} = -\frac{\pi \phi \mu_0 M_d^3 D^3}{18k(T - T_0)^2} = \frac{-\chi_0}{(T - T_0)} \tag{E-10}$$

Replacing (E-2) and (E-10) in (E-1) give

73

$$-\frac{1}{T-T_0}+\frac{2\tau^2\Omega^2KV}{kT^2(1+\tau^2\Omega^2)}=0 \qquad \text{(E-11)}$$

Grouping terms we obtain

$$\left(2KV-\frac{kT^2}{T-T_0}\right)\Omega^2\tau^2=\frac{kT^2}{T-T_0} \qquad \text{(E-12)}$$

and

$$\Omega^2\tau^2=\frac{1}{\dfrac{2KV(T-T_0)}{kT^2}-1} \qquad \text{(E-13)}$$

equating (E-5) and (E-13) and taking the reciprocal gives

$$\frac{\chi'}{\chi_0-\chi'}=\frac{2KV}{k(T-T_0)}-1 \qquad \text{(E-14)}$$

Rearranging

$$\chi_0=\frac{2KV(T-T_0)}{kT^2}(\chi_0-\chi') \qquad \text{(E-15)}$$

$$\frac{2KV(T-T_0)}{kT^2}\chi'=\chi_0\left[\frac{2KV(T-T_0)}{kT^2}-1\right] \qquad \text{(E-16)}$$

replacing the value of χ_0 (equation 3.50)

$$\frac{2KV}{k}\frac{\chi'}{T-T_0}=\frac{\pi\phi\mu_0 M_d^2 D^3}{18k(T-T_0)}\left[\frac{2KV(T-T_0)}{kT^2}-1\right] \qquad \text{(E-17)}$$

$$\frac{2KV}{k}\left(\frac{18k}{\pi\phi\mu_0 M_a^2 D^3 k}\right)\frac{(T-T_0)}{T^2}\chi' = \frac{2KV}{kT^2} - \frac{1}{T-T_0} \qquad (E\text{-}18)$$

$$\frac{T^2}{T-T_0} = \frac{2KV}{k} - \frac{2KV}{k}\left(\frac{18k}{\pi\phi\mu_0 M_a^2 D^3}\right)(T-T_0)\chi' \qquad (E\text{-}19)$$

Evaluation of $\Omega\tau$ in the peak of the out-phase component of the susceptibility with respect to frequency curve.

$$\chi'' = \frac{\chi_0 \Omega\tau}{1+\Omega^2\tau^2}$$

Taking the derivate with respective to Ω yields

$$\frac{\partial\chi''}{\partial\Omega} = \frac{\chi_0\tau(1+\Omega^2\tau^2) - 2\Omega\tau^2(\chi_0\Omega\tau)}{(1+\Omega^2\tau^2)^2} = 0$$

Which results in

$$\Omega^2\tau^2 = 1$$

Evaluation of $\Omega\tau$ in the peak of the in-phase component of the susceptibility with respect to temperature using Brownian relaxation time.

a)   Considering negligible interparticle interaction

Take the derivate of equation (3.53) with respect to temperature yields,

$$\frac{\partial \tau_B}{\partial T} = -\frac{\tau_B}{T}.$$

Replacing in equation (3.56) and assuming negligible interparticle interaction gives

$$\frac{\partial \chi'}{\partial T} = \frac{1}{1+\Omega^2\tau^2}\left(\frac{-\chi_0}{T}\right) - \frac{2\tau\Omega^2}{(1+\Omega^2\tau^2)^2}\chi_0\left(\frac{-\tau}{T}\right) = 0$$

Canceling and reorganized terms obtain

$$\Omega\tau = 1$$

b)   Considering the interparticle interaction

$$\frac{\partial \chi'}{\partial T} = \frac{1}{1+\Omega^2\tau^2}\left(\frac{-\chi_0}{T-T_0}\right) - \frac{2\tau\Omega^2}{(1+\Omega^2\tau^2)^2}\chi_0\left(\frac{-\tau}{T}\right) = 0 \qquad (6.15)$$

Collecting terms results in

$$\Omega\tau = \sqrt{\frac{T}{T-2T_0}} \qquad (6.16)$$

76

APPENDIX G

Relation between the in-phase component of the AC susceptibility χ' and temperature corresponding to the maximum T_{max}
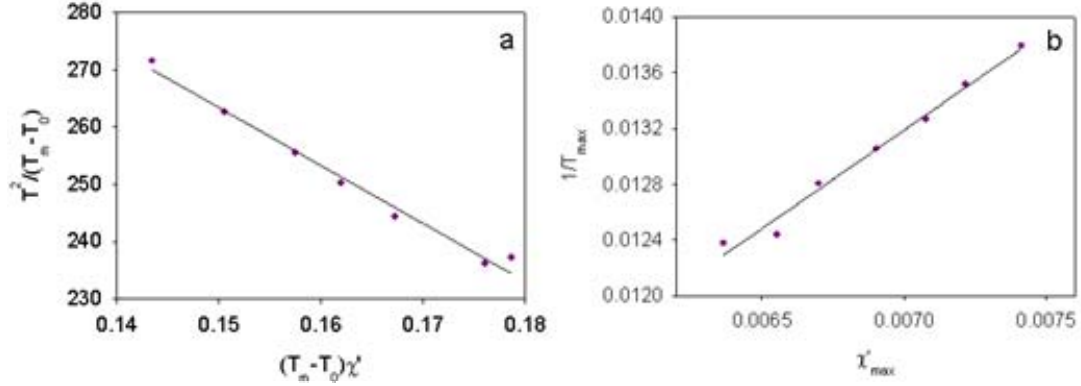
Figure 47: Relation between the in-phase component of the AC susceptibility χ' and temperature corresponding to the maximum T_{max} for the cobalt substituted ferrite prepared with Fe:Co ratio of 4:1 considering (a) interparticle interaction and (b) negligible interparticle interaction.
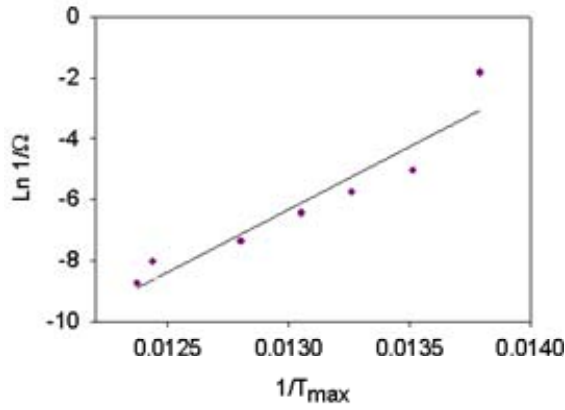
Figure 48: Relation between the inverse applied field frequency $1/\Omega_f$ and the inverse temperature Tmax corresponding to a maximum in χ' for the cobalt substituted ferrite prepared with Fe:Co ratio of 4:1
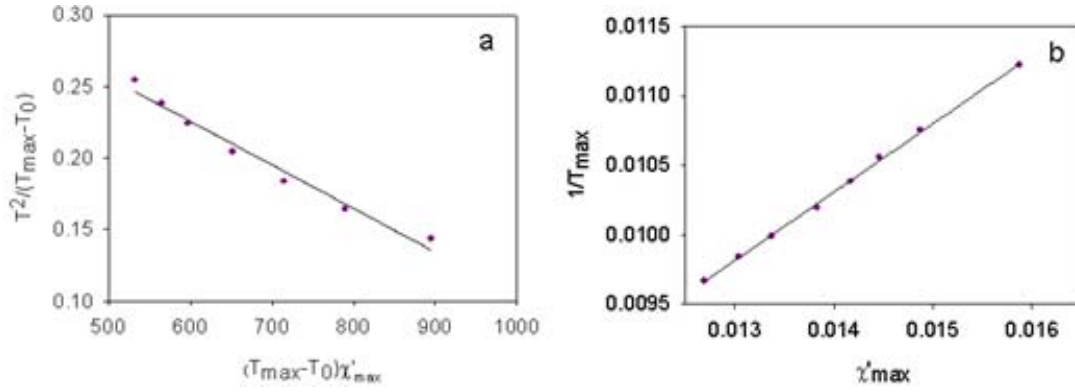
Figure 49: Relation between the in-phase component of the AC susceptibility χ' and temperature corresponding to the maximum T_{max} for the cobalt substituted ferrite prepared with Fe:Co ratio of 5:1 considering (a) interparticle interaction and (b) negligible interparticle interaction.

Figure 50: Relation between the inverse applied field frequency $1/\Omega_f$ and the inverse temperature Tmax corresponding to a maximum in χ' for the cobalt substituted ferrite prepared with Fe:Co ratio of 5:1.

BIBLIOGRAPHY

[1]   I. Safarik and M. Safarikova, "Magnetic nanoparticles and biosciences," *Monotshefte fut Chemie*, vol. 133, pp. 737, 2002.

[2]   T. Vo-Dihn, B. Cullum, and D. Stokes, "Nanosensors and biochips: frontiers in biomolecular diagnostics," *Sensors and actuators B*, vol. 74, pp. 2, 2001.
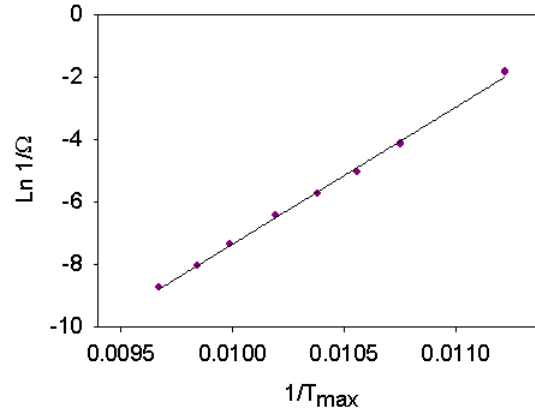
[3]   A. Haes and R. V. Duyne, "Nanosensorsenable portable detectors for enviromental and medical applications," *Laser Focus World*, vol. 39, 2003.

[4]   H. A. Clark, M. Hoyer, M. A. Philbert, and R. Kopelman, "Optical nanosensors for chemical analysis inside single living cells. 1. Fabrication, characterization, and methods for intracellular delivery of PEBBLE sensors," *Analytical Chemistry*, vol. 71, pp. 4831-4836, 1999.

[5]   J. M. Perez, L. Josephson, T. O'Loughlin, D. Hogemann, and R. Weissleder, "Magnetic relaxation switches capable of sensing molecular interactions," *Nature Biotechnology*, vol. 20, pp. 816-820, 2002.

[6]   S. H. Chung, A. Hoffmann, S. D. Bader, C. Liu, B. Kay, L. Makowski, and L. Chen, "Biological sensors based on Brownian relaxation of magnetic nanoparticles," *Applied Physics Letters*, vol. 85, pp. 2971-2973, 2004.

[7]   C. B. Kriz, K. Radevik, and D. Kriz, "Magnetic permeability measurements in bioanalysis and biosensors," *Analytical Chemistry*, vol. 68, pp. 1966-1970, 1996.

[8]   V. L. Calero-DdelC, C. Rinaldi, and M. Zahn, *Magnetic fluid and nanoparticle based sensors*, to appear in Encyclopedia of Sensors ed: C.A. Grimes, E.C. Dickey, and M.V. Pishko, Eds: American Scientific Publishers, 2005.

[9]   D. Jiles, *Introduction to Magnetism and Magnetic Materials*, First ed. ed. Londond: Chapman & Hall, 1991.

[10]   R. M. Bozorth, *Ferromagnetism*. New York: Editorial Board, 1993.

[11]   A. Goldman, *Modern Ferrite Technology*. New York: Van Nostrand Reinhold, 1990.

[12]   W. Callister, *Materials science and engineering an introduction*, Sixth ed. New York: JoHn Wiley & Sons, Inc, 2003.

[13]   M. Zhan, *Electromagnetic Field Theory: a problem solving approach*. Malabar, Florida: Krieger Publishing Company, 2003.

[14]   N. Spaldin, *Magnetic materials: Fundamentals and device applications*. Cambridge: Cambridge University press, 2003.

[15]   V. Pillai and D. O. Shah, "Synthesis of high-coercivity cobalt ferrite particles using water-in-oil microemulsions," *Journal of Magnetism and Magnetic Materials*, vol. 163, pp. 243-248, 1996.

[16]   L. D. Tung, V. Kolesnichenko, D. Caruntu, N. H. Chou, C. J. O'Connor, and L. Spinu, "Magnetic properties of ultrafine cobalt ferrite particles," *Journal of Applied Physics*, vol. 93, pp. 7486-7488, 2003.

[17]   N. Moumen and M. P. Pileni, "Control of the size of cobalt ferrite magnetic fluid," *Journal of Physical Chemistry*, vol. 100, pp. 1867-1873, 1996.

[18]   R. E. Rosensweig, *Ferrohydrodynamics*. Mineola, New York: Dover Publications, INC, 1985.

[19]   C. R. Rinaldi, "Applications of fluids containing magnetic nanoparticles," *To be published*.

[20]   G. D. Moeser, K. A. Roach, W. H. Green, P. E. Laibinis, and T. A. Hatton, "Water-based magnetic fluids as extractants for synthetic organic compounds," *Industrial & Engineering Chemistry Research*, vol. 41, pp. 4739-4749, 2002.

[21]   P. A. Voltairas, D. I. Fotiadis, and L. K. Michalis, "Hydrodynamics of magnetic drug targeting," *Journal of Biomechanics*, vol. 35, pp. 813-821, 2002.

[22]   C. Alexiou, A. Schmidt, R. Klein, P. Hulin, C. Bergemann, and W. Arnold, "Magnetic drug targeting: biodistribution and dependency on magnetic field strength," *Journal of Magnetism and Magnetic Materials*, vol. 252, pp. 363-366, 2002.

[23]   A. Halbreich, E. V. Groman, D. Raison, C. Bouchaud, and S. Paturance, "Damage to the protein synthesizing apparatus in mouse liver in vivo by magnetocytolysis in the presence of hepatospecific magnetic nanoparticles," *Journal of Magnetism and Magnetic Materials*, vol. 248, pp. 276-285, 2002.

[24]   M. Berger, J. Castelino, R. Huang, M. Shah, and R. H. Austin, "Design of an microfabricated magnetic cell separator," *Electrophoresis*, vol. 22, pp. 3883, 2001.

[25]   J. Connolly and T. G. St Pierre, "Proposed biosensors based on time-dependent properties of magnetic fluids," *Journal of Magnetism and Magnetic Materials*, vol. 225, pp. 156-160, 2001.

[26]   B. M. Berkovsky, *Magnetic fluids, Engineering Applications*. Oxford, UK, 1993.

[27]   R. W. Chantrell, J. Popplewell, and S.W.Charles, "Measurements of particle size distribution parameters in ferrofluids," *IEEE Transactions on magnetics*, vol. 14, pp. 975-977, 1978.

[28]   J. Popplewell and L. Sakhnini, "The dependencce of the physical and magnetic properties of magnetic fluids on particle size," *Journal of Magnetism and Magnetic Materials*, vol. 149, pp. 72-78, 1995.

[29]   A. Bradbury, S. Menear, K. O'Grady, and R. W. Chantrell, "Magnetic size determination for interacting fine particle systems," *IEEE Transactions on Magnetics*, vol. 20, pp. 1846-1848, 1984.

[30]   K. Raj, B. Moskowitz, and R. Casciari, "Advances in ferrofluid technology," *Journal of Magnetism and Magnetic Materials*, vol. 149, pp. 174, 1995.

[31]   N. Feltin and M. P. Pileni, "New technique for synthesizing iron ferrite magnetic nanosized particles," *Langmuir*, vol. 13, pp. 3927-3933, 1997.

[32]   S. W. Charles, "The preparation of magnetic fluids," in *Ferrofluids: Magnetically Contrallable Fluids and Their Applications*, S. Odenbach, Ed. Germany: Springer-Verlag, 2002, pp. 3-18.

[33]   B. Simmons., L. Liu, C. Taylor, D. Schwartz, G. Mcpherson, A. Bose, and V. Agarwal, *Synthesis, Funtionalization and Surface Treatment of Nanoparticles.*, 2003.

[34]   M. P. Pileni, "Nanosized particles made in colloidal assemblies," *Langmuir*, vol. 13, pp. 3266-3276, 1997.

[35]   J. Israelachvili, *Intermolecular & surface forces*, Second ed. San Diego, California, 1992.

[36]   D. Langevin, "Structure of reversed micelles," in *Structure and reactivity in reverse micelle*. New York: Elsevier, 1989, pp. 13-43.

[37]   N. Levinger, "Chemistry: water in confinement," *Science*, vol. 298, pp. 1722-1723, 2002.

[38]   G. W. Zhou, G. Z. Li, and W. J. Chen, "Fourier transform infrared investigation on water states and the conformations of aerosol-OT in reverse Microemulsions," *Langmuir*, vol. 18, pp. 4566-4571, 2002.

[39]   M. P. Pileni, "Reverse Micelles as Microreactors," *Journal of Physical Chemistry*, vol. 97, pp. 6961-6973, 1993.

[40]   S. Santra, R. Tapec, N. Theodoropoulou, J. Dobson, A. Hebard, and W. Tan, "Synthesis and characterization of silica-coated iron oxide nanoparticles in microemulsion: the effect of nonionic surfactants.," *Langmuir*, vol. 17, pp. 2900, 2001.

[41]   L. F. Shen, P. E. Laibinis, and T. A. Hatton, "Aqueous magnetic fluids stabilized by surfactant bilayers," *Journal of Magnetism and Magnetic Materials*, vol. 194, pp. 37-44, 1999.

[42]   F. Montagne, O. Mondain-Monval, C. Pinchot, H. Mozzanega, and A. Elaissari, "Preparation and characterization of narrow sized (o/w) magnetic emulsion," *Journal of Magnetism and Magnetic Materials*, vol. 250, pp. 302-312, 2002.

[43]   V. Blaskov, V. Petkov, V. Rusanov, L. M. Martinez, B. Martinez, J. S. Munoz, and M. Mikhov, "Magnetic properties of nanophase CoFe2O4 particles," *Journal of Magnetism and Magnetic Materials*, vol. 162, pp. 331-337, 1996.

[44]   I. Lisiecki and M. P. Pileni, "Synthesis of copper metallic clusters using reverse micelles as microreactors," *Journal of the American Chemical Society*, vol. 115, pp. 3887-3896, 1993.

[45]   C. J. O'Connor, V. Kolesnichenko, E. Carpenter, C. Sangregorio, W. L. Zhou, A. Kumbhar, J. Sims, and F. Agnoli, "Fabrication and properties of magnetic particles with nanometer dimensions," *Synthetic Metals*, vol. 122, pp. 547-557, 2001.

[46]   S. Li, L. Liu, V. T. John, C. J. O'Connor, and V. G. Harris, "Cobalt-ferrite nanoparticles: Correlations between synthesis procedures, structural characteristics, and magnetic properties," presented at 8th Joint Magnetism and Magnetic Materials -International Magnetic Conference- (MMM-Intermag), Jan 7-11 2001, San Antonio, TX, 2001.

[47]   N. Moumen, P. Veillet, and M. P. Pileni, "Controlled preparation of nanosize cobalt ferrite magnetic particles," *Journal of Magnetism and Magnetic Materials Proceedings of the 7th International Conference on Magnetic Fluids, Jan 7-14 1995*, vol. 149, pp. 67-71, 1995.

[48]   A. J. Rondinone, A. C. S. Samia, and Z. J. Zhang, "Characterizing the magnetic anisotropy constant of spinel cobalt ferrite nanoparticles," *Applied Physics Letters*, vol. 76, pp. 3624-3626, 2000.

[49]   E. Auzans, D. Zins, E. Blums, and R. Massarte, "Synthesis and properties of Mn-ZN ferrite ferrofluids," *Journal of materials science*, vol. 34, pp. 1253-1260, 1999.

[50]   P. Nathwani and V. S. Darshane, "Structural, transport, magnetic and infrared studies of the oxidic spinels $Co_{2-x}Ti_{1-x}Fe_{2x}O_4$," *Journal of Physics C: Solid State Physics [Proceedings of the Physical Society*, vol. 21, pp. 3191-3203, 1988.

[51]   M. Nohair, D. Aymes, P. Perriot, and B. Gillot, "Infrared specttra-structure correlation study of vanadiu-iron spinels and of their oxidation products," *Vibrational spectrocopy*, vol. 9, pp. 181-190, 1995.

[52]   B. Gillot, "Infrared spectrometric investigation of submicron metastable cation-deficient spinels in relation to order-disorder phenomena and phase transition," *Vibrational spectrocopy*, vol. 6, pp. 127-148, 1994.

[53]   N. Moumen and M. P. Pileni, "New synthesis of cobalt ferrite particles in the range 2-5nm: Comparison of the magnetic properties of the nanosized particles in dispersed fluid or in powder form," *Chemistry of Materials*, vol. 8, pp. 1128-1134, 1996.

[54]   X. Li, G. Chen, Y. Po-Lock, and C. Kutal, "Preparation and characterization of superparamagnetic nanocrystalline cobalt ferrite materials," *Journal of Materials Science Letters*, vol. 21, pp. 1881-1883, 2002.

[55]   F. Bensebbaa, F. Zavaliche, P. L'Ecuyer, R. W. Cochrane, and T. Veres, "Microwave synthesis and characterization of Co-ferrite nanoparticles," *Journal of Colloidal and Interface Science*, vol. 277, pp. 104-110, 2004.

[56]   Y. Deng, L. Wang, W. Yang, S. Fu, and A. Elaissari, "Preparation of magnetic polymeric particles via inverse microemulsion polymerization process," *Journal of Magnetism and Magnetic Materials*, vol. 257, pp. 69-78, 2003.

[57]   R. W. Cornell and U. Schewrtmann, *The Iron Oxides*, Second ed. Germany, 2000.

[58]   Y. Ahn, E. J. Choi, S. Kim, and H. N. Ok, "Magnetization and Mössbauer study of cobalt ferrite particles from nanophase cobalt iron carbonate," *Matterials Letters*, vol. 50, pp. 47-52, 2001.

[59]   Q. Song and Z. J. Zhang, "Shape control and associated magetic properties of spinel cobalt ferrite nanocrystals," *Journal of the American Chemical Society*, vol. 126, pp. 6164-6168, 2004.

[60]   S. Ammar, A. Helfen, N. Jouini, F. Fiévet, I. Rosenman, F. Villain, P. Molinié, and M. Danot, "Magnetic porperties of ultrfine cobalt ferrite particles syntehsized by hydrolisis in apolyol medium," *Journal of Materials Chemistry*, vol. 11, pp. 186-192, 2001.

[61]   Z. L. Liu, H. B. Wang, Q. H. Lu, G. H. Du, L. Peng, Y. Q. Du, S. M. Zhang, and K. L. Yao, "Synthesis and characterization of ultrfine-well dispersed magnetic nanoparticles," *Journal of Magnetism and Magnetic Materials*, vol. 283, pp. 258-262, 2004.

[62]   N. Hanh, O. K. Quy, N. P. Thuy, L. D. Tung, and L. Spinu, "Synthesis of cobalt ferrite nanocrystallites by the forced hydrolysis method and investigation of their magnetic properties," *Physica B-Condensed Matter*, vol. 327, pp. 382-384, 2003.

[63]   S. Li, C. J. O'Connor, V. G. Harris, and E. Carpenter, "Cobalt ferrite nanoparticles: Structure, cation distributions, and magnetic properties," *Journal of Applied Physics*, vol. 87, pp. 6223, 2000.

[64]   C. T. Seip, E. E. Carpenter, and C. J. O'Connor, "Magnetic properties of a series of ferrite nanoparticles synthesized in reverse micelles," *IEEE Transactions on Magnetics*, vol. 34, pp. 1111-1113, 1998.

[65]   P. Debye, *Polar Molecules*. New York, NY: Dover, 1929.

[66]   Y. L. Raikher and C. I. Stepanov, "Linear and cubic dynamic susceptibilities of superparamagnetic fine particles," *Physical Review B*, vol. 55, pp. 15005-15017, 1997.

[67]   C. T. Hsieh and J. T. Lue, "Anisotropy-induced quantum superparamagnet state in colbalt-ferrite nanoparticles at low temperatures," *Physics Letters A*, vol. 316, pp. 329-335, 2003.

[68]   X. X. Zhang, G. H. Wen, G. Xiao, and S. Sun, "Magnetic relaxation of diluted and self-assembled cobalt nanocrystals," *Journal of Magnetism and Magnetic Materials*, vol. 261, pp. 21-28, 2003.